NASA TECHNICAL NOTE

NASA TN D-5803

NASA TN D-5803

EVALUATION OF A FINITE-ELEMENT ANALYSIS FOR LONGITUDINAL VIBRATIONS OF LIQUID-PROPELLANT LAUNCH VEHICLES

by Larry D. Pinson

Langley Research Center
Hampton, Va. 23365

NATIONAL AERONAUTICS AND SPACE ADMINISTRATION • WASHINGTON, D. C. • JUNE 1970

1. Report No.	2. Government Accession No.	3. Recipient's Catalog No.
NASA TN D-5803		

4. Title and Subtitle	5. Report Date
EVALUATION OF A FINITE-ELEMENT ANALYSIS FOR LONGITUDINAL VIBRATIONS OF LIQUID-PROPELLANT LAUNCH VEHICLES	June 1970
	6. Performing Organization Code

7. Author(s)	8. Performing Organization Report No.
Larry D. Pinson	L-5385
	10. Work Unit No.
9. Performing Organization Name and Address	124-08-13-04-23
NASA Langley Research Center Hampton, Va. 23365	11. Contract or Grant No.
	13. Type of Report and Period Covered
12. Sponsoring Agency Name and Address	Technical Note
National Aeronautics and Space Administration Washington, D.C. 20546	14. Sponsoring Agency Code

15. Supplementary Notes

16. Abstract

An evaluation of a finite-element analysis for axisymmetric liquid-propellant launch vehicles has been carried out. The evaluation is performed by comparison of results from the application of the analysis to a multistage liquid-propellant launch-vehicle model with experimentally determined resonant frequencies and deflection shapes and with results from a spring-mass analysis.

A description of some of the problems encountered in this application and their solutions are presented. The methods used in preparation of the input for the associated computer program are also described.

17. Key Words (Suggested by Author(s))	18. Distribution Statement
Finite-element analysis Longitudinal vibrations Spring-mass analysis	Unclassified – Unlimited

19. Security Classif. (of this report)	20. Security Classif. (of this page)	21. No. of Pages	22. Price*
Unclassified	Unclassified	57	$3.00

*For sale by the Clearinghouse for Federal Scientific and Technical Information
Springfield, Virginia 22151

EVALUATION OF A FINITE-ELEMENT ANALYSIS FOR LONGITUDINAL VIBRATIONS OF LIQUID-PROPELLANT LAUNCH VEHICLES

By Larry D. Pinson
Langley Research Center

SUMMARY

An evaluation of a finite-element analysis for axisymmetric liquid-propellant launch vehicles is presented. The evaluation is performed by comparison of results from the application of the analysis to the 1/10-scale Saturn V replica model with experimentally determined resonant frequencies and deflection shapes and with results from a spring-mass analysis.

In this application, the finite-element analysis in comparison with the spring-mass analysis yields results of significantly higher quality in modes in which the primary motion is that of the propellants. Significantly better agreement between the finite-element analysis and experiment is achieved in the structural modes when joint effects are considered in both analyses. A primary achievement of the finite-element analysis is that it presents a more rational treatment of propellant motion than currently exists in the spring-mass analyses.

A description of some of the problems encountered in the application and their solutions are presented. The methods used in the preparation of the input for the computer program are also described.

INTRODUCTION

Longitudinal stability problems in liquid-propellant launch vehicles involving interaction of the structure and propellant (see ref. 1) have caused considerable interest in the analysis of the longitudinal vibration characteristics of these vehicles. One approach to predicting the vibration characteristics employs the spring-mass representation; that is, the launch vehicle, including the propellants, is modeled mathematically by a number of concentrated masses located at selected stations and connected by linear massless springs. (See, for example, refs. 1, 2, and 3.) Usually, the vehicle structure can be adequately modeled in this manner except for the liquid propellant and associated containers. Some effort has been made to develop adequate procedures for simulating propellants and tanks with simple spring-mass oscillators. An example of such a study is presented in

reference 4. However, even with improved tankage representations, the simple spring-mass idealization does not give accurate and reliable results for vibration characteristics when the motion is primarily that of liquid propellants. (See ref. 3.)

Recently, a finite-element analysis for longitudinal vibrations of liquid-propellant launch vehicles was developed. The analysis and associated computer program are described in references 5, 6, and 7. In contrast to the spring-mass analysis, the finite-element analysis models the vehicle as continuous orthotropic shell elements, continuous fluid elements, and spring-mass elements. In references 8 and 9, the finite-element analysis was applied to compute the longitudinal natural modes and frequencies of models representative of liquid-propellant launch vehicles, and the results were compared with experiment. Reference 8 presents results of a study of the longitudinal vibration characteristics of a scale model of an operational launch vehicle. The model in reference 9 is a 1/10-scale model of the Apollo/Saturn V launch vehicle. Reference 9 also gives results of calculations of the modes of this model by the spring-mass method. In reference 3 the spring-mass analysis of reference 9 was expanded, and its results were compared with experiment.

Results of references 3 and 9 and of subsequent studies indicated that the effect of flexibility in certain joints should be included in the stiffness representation. Therefore, in an effort to more fully evaluate the finite-element analysis, both the spring-mass analysis of reference 3 and the finite-element analysis of reference 9 were expanded and refined, and a more comprehensive study was undertaken. The results of this study, which includes data from both the finite-element and spring-mass analyses, are presented in this report and compared with experimental data from reference 3. Frequencies determined by both analyses in which joint flexibility is not included are also presented to show the significance of this effect.

SYMBOLS

A_r, A_s	area of rings and stringers, respectively
a	ring stiffener spacing
b	stringer stiffener spacing
C_{ij}	orthotropic elastic constants (See eqs. (3) to (8))
E	Young's modulus of elasticity

f_e, f_s, f_f	frequencies determined by experiment, spring-mass analysis, and finite-element analysis, respectively
I_ϕ, I_θ	area moments of inertia
$[K_{ij}]$	stiffness matrix
k_i	spring constants, where $i = 1,2,\ldots 32$
L	model length
M_ϕ, M_θ	bending moments
m_i	concentrated mass, where $i = 1,2,\ldots 29$
$[m_{ij}]$	mass matrix
N_ϕ, N_θ	in-plane direct stress resultants
$\{q\}$	modal displacement vector
t	shell thickness
u_i	displacement of concentrated mass, where $i = 25, 26, 27$
x	distance along model measured from 0.254 meter aft of the S-IC gimbal plane
$\epsilon_\phi, \epsilon_\theta$	in-plane direct strains
$\kappa_\phi, \kappa_\theta$	changes in curvature
μ	Poisson's ratio
ω	natural circular frequency

THE FINITE-ELEMENT MATHEMATICAL MODEL

Although the finite-element analysis and the associated digital program are described in references 5 and 6, a brief description will be given here for completeness.

The launch vehicle is assumed to be comprised of three basic types of elements, as shown in figure 1. The three elements are axisymmetric shell elements of conical and ellipsoidal configuration, of which the cylindrical and spherical shells are special configurations, axisymmetric spring-mass elements, and liquid elements. A liquid element is contained within three shells but does not necessarily contact all three.

Figure 2 shows a coordinate system applicable to the illustrative finite-element model. Each coordinate in the analysis, unless constrained to be zero, represents a degree of freedom. Three coordinates, longitudinal and radial displacements and rotations, are necessary at each shell juncture. There may be additional coordinates which are interpreted as longitudinal and radial displacements in the interior of the shell elements. A radial displacement is a change in radius of the shell. Use of the same coordinates at a juncture represents a joining along the entire circumference.

The axisymmetric shell elements are assumed to have orthotropic properties. These properties may vary along the meridian of the shell. The stress resultants are related to the strains by the equation

$$\begin{Bmatrix} N_\phi \\ N_\theta \\ M_\phi \\ M_\theta \end{Bmatrix} = \begin{bmatrix} C_{11} & C_{12} & 0 & 0 \\ C_{12} & C_{22} & 0 & 0 \\ 0 & 0 & C_{33} & C_{34} \\ 0 & 0 & C_{34} & C_{44} \end{bmatrix} \begin{Bmatrix} \epsilon_\phi \\ \epsilon_\theta \\ \kappa_\phi \\ \kappa_\phi \end{Bmatrix} \tag{1}$$

In-plane shearing stresses and twisting moments are zero as a result of the assumption of axial symmetry. As the zeros in the matrix of elastic constants indicate, there is no coupling between membrane-stress resultants and changes in curvature.

The liquid is assumed to be incompressible and inviscid. The displacements in a liquid element are determined by rules based on the following assumptions: (1) The volume of a liquid element is constant. (2) A plane through the liquid perpendicular to the longitudinal axis of the vehicle before deformation is assumed to remain planar and to remain perpendicular to the longitudinal axis after the deformation. (3) The radial motion of the liquid is assumed to vary linearly from zero at the center line of the tank to a value equal to the radial displacement of the shell at the wall. As a result, free-surface effects are excluded and a liquid element does not add degrees of freedom to the model.

Stiffness and mass matrices for shell elements and mass matrices for liquid elements are computed internally by applying the Rayleigh-Ritz method. The assumed displacement functions for the shells are polynomials. Static prestress is taken into account in computing shell stiffnesses. Stiffness and mass matrices for spring-mass elements are entered directly. Stiffness and mass matrices of the complete launch vehicle are

obtained by superposition of the stiffness and mass matrices of the individual elements. Compatability of displacements and rotations is maintained at the junctures. When the stiffness and mass matrices are assembled, the natural frequencies and mode shapes are found from an eigenvalue problem of the standard form

$$\left([K_{ij}] - \omega^2[m_{ij}]\right)\{q\} = \{0\} \tag{2}$$

where $[K_{ij}]$ is the stiffness matrix, $[m_{ij}]$ is the mass matrix, ω is the natural circular frequency, and $\{q\}$ is the modal displacement vector whose elements are the coordinates described in connection with figure 2.

The computer program is limited to a maximum of six fluid elements, 30 spring-mass elements, and 40 shell elements. The stiffness and mass matrices for a spring-mass element are each limited to order 10. Up to 11 polynomials of order 10 or less can be used to describe the motion of a shell element. A maximum of 80 degrees of freedom is allowed.

The complete description of a shell element requires specification of the coordinates associated with that shell, the geometry of the shell, the mass density, total mass, preload data, and distributions of six orthotropic shell-stiffness parameters. A cubic distribution is assumed for the bending stiffnesses, and this distribution is described by specification of the bending stiffnesses at the ends of the shell and at the one-third points along the meridian. A linear distribution is assumed for the in-plane stiffnesses, and this distribution is described by specification of the in-plane stiffnesses at the ends of the shell. For a complete description of a liquid element, the mass density, the total mass, and the height of the liquid are required. The spring-mass elements require the specification of the coordinates of the masses, the mass values, and the stiffness matrix.

The output of the digital program includes the mass and stiffness matrices, the frequencies, and the mode shapes, given as the longitudinal and radial displacements and rotations at specified locations on the vehicle.

ANALYTICAL PROCEDURES

Both the finite-element analysis and the spring-mass analysis of reference 3 have been applied to the 1/10-scale model of the Apollo/Saturn V launch vehicle. The procedures used in the finite-element analysis are summarized herein and a brief description of the spring-mass analysis is presented. Figure 3 is a photograph of the 1/10-scale model of the Apollo/Saturn V launch vehicle, and figure 4 is a line drawing on which various subassemblies are labeled. Nomenclature corresponding to the full-scale Saturn V vehicle is used. A complete description of the 1/10-scale model is presented in

reference 10. Three weight conditions were analyzed, 100-percent propellant in the S-IC stage (lift off), 50-percent propellant in the S-IC stage, and S-IC stage empty.

Description of Analytical Models

The elements and the coordinates of the finite-element representation are shown in figure 5, and figure 6 shows the spring-mass model of reference 3. As shown in figure 5, the finite-element model consisted of 29 shell elements, 6 liquid elements, and 5 spring-mass elements. A total of 79 coordinates resulted of which 39 were longitudinal, 20 were radial, and 20 were rotational. Additional longitudinal degrees of freedom were introduced at three joints in order to account for joint flexibility. Joint flexibility is discussed further in the section entitled "Results and Discussion." The simulated lunar module was represented as a two-degree-of-freedom spring-mass system. All engines were represented as axisymmetric spring-mass attachments to the main structure.

The spring-mass model (fig. 6) had 29 degrees of freedom in the 100-percent- and 50-percent-weight conditions and 27 degrees of freedom in the empty condition. Table I gives the values of each of the spring constants and masses used in the spring-mass model. Spring constants listed in this table reflect the same joint flexibility as that of the finite-element analysis.

Orthotropic Constants

The greatest task of the application was the calculation of orthotropic elastic constants for each of the shell elements. A typical shell component of the Saturn V model consists of a skin which may have a variable thickness and both longitudinal and circumferential stiffeners. A typical repeating element of a shell of this type is shown in figure 7. In order to calculate the stiffness parameters for such a configuration in a form which is compatible with the program, the following assumptions are made: (1) The stiffened shell can be represented by an axisymmetric orthotropic thin shell. (2) The behavior of the equivalent shell is described by equation (1) in that eccentricity effects are ignored. (3) The constants of proportionality are taken to be

$$C_{11} = \frac{Et}{1 - \mu^2} + \frac{A_S E}{b} \tag{3}$$

$$C_{12} = \frac{\mu Et}{1 - \mu^2} \tag{4}$$

$$C_{22} = \frac{Et}{1 - \mu^2} + \frac{A_r E}{a} \tag{5}$$

$$C_{33} = \frac{EI_{\phi}}{b(1 - \mu 2)} \tag{6}$$

$$C_{34} = \frac{\mu Et^3}{12(1 - \mu 2)} \tag{7}$$

$$C_{44} = \frac{EI_{\theta}}{a(1 - \mu 2)} \tag{8}$$

where I_{ϕ} is the area moment of inertia of a typical repeating shell element about the composite centroid in the meridional direction and I_{θ} is the corresponding area moment of inertia in the circumferential direction. The expressions for C_{12} and C_{34} are computed as though the stiffeners are not present. An example of the calculation of the orthotropic stiffness parameters is given in the appendix. Table II presents the complete set of the orthotropic shell elastic constants used in the application to the Saturn V model. The effect of variations in the bending parameters is discussed subsequently.

Shells Containing Liquid

The finite-element computer program requires specification of three shells for the containment of a liquid element. The Saturn V model has six propellant tanks of which two are constructed so that only two shells contain the liquid. In order to treat this system without modifying the program, the geometry of these tanks was modified in the idealization process. Figure 8 shows drawings of the actual and idealized S-II stage and S-IVB stage liquid oxygen tanks.

The S-IVB stage liquid oxygen tank shown in figure 8(a) is comprised of two bulkheads, the lower bulkhead, which is hemispherical, and the upper bulkhead, which is a 70° spherical cap. The upper bulkhead is a common bulkhead, separating the liquid oxygen tank from the liquid hydrogen tank, and is attached to the lower bulkhead rather than to the vehicle outer wall. A fairly extensive and somewhat arbitrary modification was used in order to fit this lox tank into the format of the computer program. The modification which was made is shown as the idealized tank. In place of the upper bulkhead, an ellipsoidal bulkhead was used which had the same minor-axis length as the middle ordinate of the spherical cap and a major-axis length equal to the radius of the vehicle outer wall. Consequently, the idealized upper bulkhead is joined to the vehicle outer shell rather than directly to the lower bulkhead. A short cylindrical shell of arbitrarily chosen length was inserted between the junction of this ellipsoidal bulkhead and the vehicle outer shell and the junction of the lower bulkhead to the vehicle outer shell. This modification yields a configuration for the lox tank which is made up of three shells, thus satisfying the format requirements of the computer program.

Figure 8(b) shows a drawing of the actual and idealized liquid oxygen tank of the S-II stage. The actual tank is made up of two ellipsoidal bulkheads. The upper bulkhead is common to both the liquid oxygen and liquid hydrogen tanks in this stage also. The modification which was made was the insertion of a short cylindrical section at the junction so that the liquid in the tank was contained by three shells, two ellipsoidal and one cylindrical.

The stiffness used for each inserted cylinder was the same as that of the adjacent vehicle outer shell. The use of these inserted cylinders results in an analytical model slightly longer than the actual launch vehicle model.

Simulated Lunar Module

Initial tests on the 1/10-scale model indicated a resonant response of the simulated lunar module (LM) at approximately 70 hertz, which was not predicted by the initial analysis. Studies were performed, therefore, to determine the reasons for this discrepancy.

A photograph and a line drawing of the lunar module are shown in figures 9 and 10, respectively. This component consists of an aluminum cylinder with end plates attached. The end plates have cutouts and are connected by two bolts near the plate center. Internal ballast weights are attached at the aft end of each bolt; and, in addition, small plates are added to the exterior for additional weight. Four sets of supporting struts are attached to the cylinder and serve to attach the simulated lunar module to its conical adapter.

In the initial analysis of the 1/10-scale model, the flexibility of the LM was assumed to come only from the supporting struts, and the LM was represented with one degree of freedom. Separate tests on this component, which are discussed in reference 3, showed that while the calculations for the stiffness of the supporting struts were accurate, the primary deformation was in the top and bottom end plates. A new representation was made of this component which accounted for the motion of the end plates and an uncoupled natural frequency of the proper magnitude resulted. In this new analysis, the component was treated as a two-degree-of-freedom model. Thus, a spring-mass system was found which had the proper natural frequency but only after experimental evidence indicated improper assumptions in the original calculations.

RESULTS AND DISCUSSION

In this section, results of the application of the finite-element analysis to the 1/10-scale Saturn V model are presented. These results are compared with experimental data from reference 3 and with results of the spring-mass analysis. Figures 11 and 12 are summary plots of calculated natural frequencies from the spring-mass analysis and

finite-element analysis, respectively. The frequencies are plotted as a function of the amount of propellant in the S-IC stage. Experimental and analytical natural frequencies and mode shapes are presented in figures 13 to 20. Only longitudinal displacements are shown in the figures. An experimental natural frequency is taken to be the frequency at which a relative maximum value of longitudinal acceleration occurs on a plot of absolute acceleration response as a function of excitation frequency at a constant harmonic force amplitude. The experimental data were harmonically analyzed, as discussed in reference 3. The experimental data points shown in the figures are amplitudes of the fundamental harmonics. These displacement shapes are called experimental mode shapes. The format for presentation of data is the same for all the figures. Experimental data are presented by open symbols. The responses measured on the main structure are connected with a solid line. The results from the spring-mass analysis are presented by partially darkened symbols for branch-mass deformation and a dashed line for main-structure deformation. The results from the finite-element analysis are presented by completely darkened symbols for the branch-mass deformation and a long-and-short dashed line for main-structure deformation. The symbols f_e, f_s, and f_f are used to indicate natural frequencies from experiment, spring-mass analysis, and finite-element analysis, respectively. Both experimental and analytical mode shapes are normalized to unity at the top of the spacecraft.

In addition to the summary plots of figures 11 and 12, a frequency summary is presented in table III. For each analysis, two values are given for the natural frequency associated with each predicted mode. The first value is the natural frequency calculated with joint flexibility included, and the second value is the result not including joint flexibility. One result is that joint flexibility significantly affects the frequencies for the structural modes but does not significantly change the frequencies for the liquid-structure-interaction modes. In reference 11 an analysis which included the effect on frequencies of joint flexibility in the Saturn V model is presented. These effects were incorporated on the basis of static tests on the model reported in reference 3. It was found for the first and second structural modes that approximately a 10-percent decrease in calculated frequency was possible. Vibration tests were conducted at Langley Research Center to determine the effect of axial preload on the frequencies of the Saturn V model. These tests are reported in reference 12. For the first structural mode in an off-loaded weight condition, preload was found to cause an increase in the frequency by about 8 percent. This increase is attributed to the tightening of structural joints as preload is applied. The measured frequencies of the Saturn V model, reported in references 3 and 9 and used in the present paper, were obtained with no preload. Only one joint effect, that at the base of the instrument unit, was accounted for in the spring-mass analysis of reference 3.

In view of the experimental data, a comparison of analysis and experiment should account for joint flexibility. Either the experimental frequencies of reference 3 should

be raised based on the experimental preload studies or the analyses should approximate these effects in some rational manner based on static tests which show joint effects. In this paper, joint-flexibility effects are approximated in the analyses. Three linear springs are introduced which were calculated from the static test data presented in reference 3. The spring constants given in table I reflect these springs. The joint springs were used to connect the longitudinal degrees of freedom at the joints where two longitudinal coordinates are shown in figure 5. Results of analyses in which the springs are incorporated are used for the summary plots of figures 11 and 12.

In table III for the 100-percent-weight condition, a column headed spring-mass (equivalent) is shown. These frequencies have been computed by the spring-mass analysis but with liquid masses changed to equivalent values according to the procedure discussed in references 3 and 9. The analysis incorporating equivalent masses was conducted only for the 100-percent-weight condition.

A noticeable feature of the comparison shown by table III is that the natural frequencies predicted by the finite-element analysis are consistently higher, except for the first S-IC lox mode (fig. 13), than those predicted by the spring-mass model. This feature is common to all weight conditions analyzed. Such a difference could arise from two sources: Accounting for the bending stiffness in each of the shells would cause an increase in frequency; and differences in the treatment of the mass could cause the difference. In the spring-mass analysis, the mass was lumped somewhat arbitrarily, whereas in the finite-element analysis, the mass matrix was obtained from the kinetic energy in a manner consistent with the Rayleigh-Ritz method. As a check on the effect of bending stiffness, the computer program was run with all bending constants set equal to zero giving results from momentless (linear membrane) orthotropic shell theory. It was found that this procedure introduced no anomalies in the program execution. As discussed in reference 3, momentless orthotropic shell theory was used to calculate the spring constants for the spring-mass analysis. As expected, the frequencies generated under this condition were all lower than the corresponding frequencies found using finite bending-stiffness parameters, but only slightly lower. The maximum difference for the first eight calculated natural frequencies was 0.5 percent for the 100-percent-weight condition. Differences in the calculated mode shapes were almost undetectable. Differences in the frequencies generated by the two analyses, therefore, appear to stem from the different methods of representing the mass.

If momentless theory is deemed adequate, a significant saving in time for input-data preparation will result since the necessity for calculating neutral surface position and moments of inertia for the various shell elements is eliminated. For the 1/10-scale Saturn V model, it is felt that momentless theory is adequate. The adequacy of the momentless theory was not known prior to the application, however.

First S-IC Lox Mode

For the 100-percent-weight condition, the lowest mode of the model involves an interaction of the liquid in the S-IC stage lox tank with the structure. Results for this mode are shown in figure 13(a). The spring-mass analysis indicates that the center of gravity of the mass of liquid in the S-IC stage lox tank moves out of phase with the structure and the centers of gravity of the remaining liquid masses move in phase with the structure. The displacement of the liquid center of gravity was not determined experimentally; but it was determined experimentally that the phases of the various liquid masses relative to the structure were in agreement with those predicted by the spring-mass analysis. The finite-element computer program does not output the displacements of the liquid masses, but since all the structural response calculated by this analysis is positive, it may be inferred that some liquid mass is moving out of phase with the structure. This lack of capability of the program in its present form to output information about the liquid displacements is regarded as a serious deficiency. There are differences in detail among the two analytical mode shapes, but they are in substantial agreement regarding the trend in the variation of the longitudinal displacement. The frequencies predicted by the finite-element analysis and the spring-mass analysis are, respectively, 7 percent and 23 percent higher than the measured frequencies. The reason for the large error in the frequency predicted by the spring-mass analysis, as discussed in reference 3, is the use of a total liquid mass with the liquid center-of-gravity displacement as a generalized coordinate to describe the liquid motion. While the use of a consistent mass value improves the frequency agreement for the lox mode, it also results in a frequency prediction for the first structural mode of 37.3 hertz (table III), which is 7 percent lower than the frequency measured for this mode, and it further degrades the correlation of the spring-mass analysis with experiment for the second structural mode.

For the 50-percent-weight condition, the spring-mass analysis yields a natural frequency at 62.8 hertz (fig. 13(b)) in which there is substantial displacement of the center of gravity of the first stage lox relative to the main structure. The finite-element analysis gives a mode at 74.9 hertz with a similar shape for the main structure. The lox motion predicted by the finite-element analysis for this mode was not determined. These two calculated modes are identified as the first S-IC lox mode for the 50-percent-weight condition. Experimentally, one resonant peak was detected at 71.2 hertz. The corresponding measured shape is shown in figure 18, as the LM mode. However, as discussed in reference 3, there is clear evidence from the trends of the experimental frequencies that the model has two nearly equal natural frequencies in the vicinity of 71.2 hertz. The finite-element analysis confirmed and aided in detecting this situation. The spring-mass analysis on the other hand, resulted in a misrepresentation of the situation, giving only one frequency in the vicinity of the correct value. The finite-element analysis predicts a displacement of the LM which is out of phase with the displacement of the structure at

the LM attachment point, whereas in the spring-mass analysis the motion of the LM and the structure at the attachment point are in phase. This difference is consistent with the fact that the lox mode frequency predicted by the finite-element analysis is higher than the uncoupled LM frequency while the lox mode frequency predicted by the spring-mass analysis is lower than the uncoupled LM frequency. Additional considerations relating to the presence of two modes in the vicinity of 71.2 hertz are discussed subsequently in connection with the LM mode.

S-II Fuel Mode

The modes shown in figure 14 identified as the S-II fuel modes come solely from the finite-element analysis. These modes were not detected experimentally and were not predicted by the spring-mass analysis. There is no significant change in either natural frequency or deformation shape with a change in S-IC stage weight condition. Although the plots do not indicate it, the modes have significant radial motion in the S-II fuel-tank area. In the Saturn V model, the liquid hydrogen is simulated with small plastic beads which have the same bulk unit weight as liquid hydrogen. Because of high damping associated with the motion of the beads and because it is questionable whether the beads behave dynamically as a liquid, it is not surprising that these modes are not found experimentally. In order to verify that this resonance involved an interaction between the S-II stage simulated liquid hydrogen, a calculation was performed in which the circumferential membrane constant C_{22} of the S-II stage fuel-tank cylinder was decreased by a factor of two. The circumferential membrane stiffness is a critical parameter in propellant-structure interaction modes. As a result of the calculation, the 39.1-hertz resonance shown in figure 14(a) was changed to 29.6 hertz, which indicates that this resonance, and presumably those shown in figures 14(b) and 14(c), is associated with deformation of the fuel tank of the S-II stage and its simulated liquid. The other resonances were unchanged.

First Structural Mode

Data for the first structural mode are shown in figure 15. As indicated previously, the natural frequencies generated by the spring-mass analysis agree more closely with the experimental natural frequencies than those of the finite-element analysis. The agreement of the deformation shape with experimental data is approximately equivalent between the two analyses. For the 100-percent-weight condition, the spring-mass analysis indicates significant motion of both the fuel and lox masses in the S-IC stage. Very little interaction between the structure and liquids is evident in the modes for the 50-percent-weight and empty conditions.

S-IVB Fuel Mode

The S-IVB fuel modes shown in figure 16 come solely from the finite-element analysis. These modes were not detected experimentally and were not predicted by the spring-mass analysis. There is no significant change in natural frequency for the different weight conditions. Although the plots do not indicate it, the modes have significant radial motion in the S-IVB stage fuel-tank area. A condition similar to that of the S-II fuel mode was suspected. To verify that the resonance involved an interaction between the S-IVB stage simulated liquid hydrogen and its container, a calculation was performed in which the circumferential membrane constant C_{22} of the fuel-tank cylinder was decreased by a factor of two. As a result of this calculation, the 51.3-hertz frequency of figure 16(a) was reduced to 39.0 hertz. The other frequencies in the 100-percent-weight condition were unchanged. It was concluded, therefore, that this resonance results from an interaction of the S-IVB stage simulated liquid hydrogen with its container.

Second Structural Mode

Figure 17 presents the second structural mode for the three weight conditions. For the 100-percent- and 50-percent-weight conditions, the frequencies from the finite-element analysis are in good agreement with experiment, and the frequencies from the spring-mass analysis are in fair agreement. For the empty condition, the frequency from the finite-element analysis is in fair agreement with experiment, and the frequency from the spring-mass analysis is in poor agreement. All natural frequencies for this mode from the spring-mass analysis are lower than experimental values. In the 100-percent- and 50-percent-weight conditions, there is little difference between the agreement of the mode shape from the spring-mass analysis with experiment and the agreement of the mode shape from the finite-element analysis with experiment. In the empty condition, the mode shape from the finite-element analysis is considered slightly better than the mode shape from the spring-mass analysis because of the closer agreement with experiment in the region of the aft end.

LM Mode

The resonances associated with large deformation of the LM relative to the main structure are shown in figure 18. The natural frequencies predicted by both analyses agree well with experimental values. A prominent characteristic of this comparison is that neither analysis predicts a deflection shape in favorable agreement with experiment.

As indicated in the discussion of the first S-IC lox mode, the experimental data of reference 3 indicate that both the lox mode and the LM mode participate in the single experimental response peak at 71.2 hertz in the 50-percent-weight condition. This

indication is strengthened by results of the finite-element analysis, which predicts natural frequencies at 69.7 hertz (LM mode) and 74.9 hertz (first S-IC lox mode). The experimental deformation shape of figure 18(b) exhibits characteristics of both these analytical mode shapes. It is also true that the experimental deformation shape of figure 18(b) exhibits characteristics of both the S-IC lox mode and the LM mode calculated by the spring-mass analysis; however, the spring-mass-analysis frequency for the first S-IC lox mode in the 50-percent-weight condition is considerably lower than the experimental frequency.

For the 100-percent-weight and the empty conditions, the experimental deformation shape indicates large motion in the aft end of the vehicle which is not shown by either analysis. There is evidence that this discrepancy is associated with response of a pressure-volume compensator in the vehicle which is not accounted for in either analysis. (See ref. 3.)

Third Structural Mode

The resonance called the third structural mode, shown in figure 19, was found by both analyses but was not found experimentally. The associated frequencies are somewhat different but, in general, the deflection shape agreement between the two analyses is fair for the 100-percent- and 50-percent-weight conditions. For the empty condition, agreement between the two analyses is poor for $x/L < 0.4$. The number of nodes in the deflection shape is consistent with a third structural resonance and all efforts to isolate a single source for the mode, such as a liquid element, have proved unsuccessful.

Second S-IC Lox Mode

The resonance called the second S-IC lox mode, shown in figure 20, results solely from the finite-element analysis. Examination of figure 12 shows that the frequency for this mode changes quite rapidly with S-IC stage propellant loading. Based on experience with the first S-IC lox mode, this rapid change suggests that the resonance results from a liquid-structure interaction. Separate calculations were made with the finite-element analysis in which the circumferential-membrane elastic constant was doubled for the S-IC stage lox tank. Significant changes resulted in both the S-IC lox mode frequency and the mode described in figure 20. A similar calculation was made in which the circumferential-membrane elastic constant was doubled for the S-IC stage fuel tank. No significant changes occurred in any of the modes in the frequency range considered in this report. It is concluded, therefore, that the source of this resonance is an interaction of the S-IC stage lox simulant with the structure.

A possible reason for not finding this mode experimentally is that, like the first S-IC lox mode, the second mode was difficult to excite and the presence of the lox suction duct resonance, and the pressure-volume compensator resonance (ref. 3) may have masked its presence. The spring-mass analysis could not predict this mode since the propellant is modeled with only one degree of freedom.

CONCLUDING REMARKS

A finite-element method for analysis of longitudinal vibrations of axisymmetric launch vehicles has been evaluated. The method has been used to calculate the longitudinal modes and frequencies of a 1/10-scale model of the Apollo/Saturn V launch vehicle. Comparisons of the finite-element-analysis results, spring-mass-analysis results, and experimental data have been made.

For the important first S-IC lox mode and the second structural mode, the finite-element analysis yielded significantly more accurate frequencies than the spring-mass analysis. The spring-mass analysis gave somewhat better frequency results than the finite-element analysis for the first structural mode.

In the frequency range considered, three more modes are predicted by the finite-element analysis than are predicted by the spring-mass analysis. These modes, all liquid-structure-interaction modes, are the S-II fuel mode, the S-IVB fuel mode, and the second S-IC lox mode. None of these additional modes were found experimentally. In the two modes involving the S-II stage and S-IVB stage fuel tanks, the plastic spheres used in the tests for liquid-mass simulation apparently precluded the existence of realistic liquid-structure-interaction modes. The reason, however, for the failure of the spring-mass analysis to predict these two modes is not apparent. For the second S-IC lox mode, the spring-mass analysis could not be successful since the propellant is modeled with only one degree of freedom; therefore, no liquid-structure-interaction modes higher than the fundamental can be predicted.

It was found necessary in both analyses to include joint characteristics to obtain accurate prediction of structural modes. Inclusion of joint effects had no significant effect on liquid-structure-interaction modes.

Although the finite-element analysis was developed by using a bending theory for shells, the program will execute correctly with only membrane-stiffness input for each shell. This flexibility permits the use of a momentless (linear membrane) shell theory when such a shell theory is felt to be adequate. Thus, the effort of calculating the bending stiffnesses, which involves a more complicated procedure than calculating the membrane

stiffnesses, is eliminated. For the 1/10-scale Saturn V model, the momentless orthotropic shell theory yielded natural frequencies only slightly lower than those found by using finite bending-stiffness parameters with no change in corresponding mode shapes.

The natural frequencies predicted by the finite-element analysis were generally higher than those predicted by the spring-mass analysis. This difference appears to stem from the method in which the mass matrix is derived. The mass matrix in the finite-element analysis is consistent with the Rayleigh-Ritz method and thus for a given mathematical model, natural frequencies obtained by this procedure are always upper bounds of the exact values. In the spring-mass analysis, the mass matrix is obtained by a somewhat arbitrary lumping and no statement concerning the bounds of the frequencies can be made.

A difficulty in applying the finite-element analysis arises for a liquid element contained by two shells instead of the required three. This difficulty occurred for two liquid elements in the application to the 1/10-scale Saturn V model. To overcome this deficiency, a modification to the structural geometry is required. No obvious degradation to the results presented herein occurred. However, the problem is considered to be relatively serious. In spite of this deficiency and the fact that the computer program does not compute a quantity which shows the resultant longitudinal liquid motion, it is felt that a more rational treatment of the propellant motion than currently exists for spring-mass analyses is a primary achievement of the finite-element analysis. The use of this procedure for representing liquid elements improved the agreement between analysis and experiment. This improved correlation is significant since propellants generally account for a very large percentage of the total weight of a launch vehicle.

Langley Research Center,
National Aeronautics and Space Administration,
Hampton, Va., March 13, 1970.

APPENDIX

TYPICAL CALCULATION OF ORTHOTROPIC STIFFNESS PARAMETERS

Typical calculations are presented here for each of the orthotropic elastic constants used in the finite-element analysis. The purposes of showing typical calculations are to illustrate the general level of sophistication of the structural theory used to obtain the computer program input and to illustrate the nature of the approximations which are necessarily made in the idealization process.

The component selected for the illustration is the S-II stage fuel-tank cylinder, which is shell number 15 in the analysis (see fig. 5). This shell is thin-skin construction with rectangular-pattern waffle stiffening. The stiffener directions are longitudinal and circumferential. The shell's construction is shown in figure 21. In addition to the waffle stiffening, ring-frame assemblies are placed on the inside of the shell as baffles. These frames act as stiffeners in the circumferential direction in addition to the skin and waffles. All material is aluminum ($E = 6.895 \times 10^{10}$ N/m2, $\mu = 0.3$). The radius of the shell is 0.5029 meter and the length is 1.3691 meters.

Calculations for the quantities needed to determine C_{11} and C_{33} (eqs. (3) and (6)) are shown in the following table:

Component of shell	Quantity	Total area, m^2	Distance to c.g., m (a)	Centroidal moment of inertia, m^4	Static moment, m^3	Parallel-axis transfer term, m^4
Skin	1	1.2039×10^{-3}	1.905×10^{-4}	0.1456×10^{-10}	2.2935×10^{-7}	0.4369×10^{-10}
Waffle	108	.1317	20.955	1.2903	2.7596	5.7827
Total		1.3356×10^{-3}		1.4359×10^{-10}	5.0531×10^{-7}	6.2196×10^{-10}

[a]Distance is measured from outside of skin.

By substituting quantities from the previous table, equations (3) and (6) yield

$$C_{11} = \frac{6.895 \times 10^{10}}{2\pi \times 0.5029}\left[\frac{1.2039}{1 - (0.3)^2} + 0.1317\right]10^{-3} = 3.174 \times 10^{7} \text{ N/m}$$

$$C_{33} = \frac{6.895 \times 10^{10}}{2\pi \times 0.5029\left[1 - (0.3)^2\right]}\left[6.2196 + 1.4359 - \frac{(5.0531)^2}{13.356}\right]10^{-10} = 13.772 \text{ N-m}$$

APPENDIX

Calculations for the quantities needed to determine C_{22} and C_{44} (eqs. (5) and (8)) are shown in the following table:

Component of shell	Quantity	Total area, m^2	Distance to c.g., m (a)	Centroidal moment of inertia, m^4	Static moment, m^3	Parallel-axis transfer term, m^4
Skin	1	5.2161×10^{-4}	1.905×10^{-4}	0.0631×10^{-10}	0.9937×10^{-7}	0.1893×10^{-10}
Waffles	14	.1341	20.955	.1314	.2811	.5890
End ring frame	1	.0095	59.690	.0703	.0570	.3402
End ring frame	1	.0055	117.475	.0021	.0644	.7568
End ring frame	1	.0055	128.270	----------	.0703	.9023
Intermediate ring frame	13	.1946	81.280	3.5192	1.5816	12.8548
Intermediate ring frame	13	.0713	165.735	.0277	1.1815	19.5820
Intermediate ring frame	13	.0713	176.530	----------	1.2585	22.2160
Added end skin	1	.0622	6.731	----------	.0419	.0282
Total		5.7701×10^{-4}		3.8138×10^{-10}	5.5300×10^{-7}	57.4586×10^{-10}

[a]Distance is measured from outside of skin.

By substituting quantities from the previous table, equations (5) and (8) yield

$$C_{22} = \frac{6.895 \times 10^{10}}{1.3691}\left[\frac{0.5216}{1 - (0.3)^2} + 0.05541\right]10^{-3} = 3.166 \times 10^{7} \text{ N/m}$$

$$C_{44} = \frac{6.895 \times 10^{10}}{1.3691\left[1 - (0.3)^2\right]}\left[57.4586 + 3.8138 - \frac{(5.5300)^2}{5.7701}\right]10^{-10} = 309.77 \text{ N-m}$$

In the calculation of the membrane and bending coupling terms (eqs. (4) and (7)), the stiffening elements are assumed not be be effective. Therefore, these calculations are reduced simply to

$$C_{12} = \frac{0.3 \times 6.895 \times 10^{10} \times 0.381 \times 10^{-3}}{\left[1 - (0.3)^2\right]} = 0.866 \times 10^{7} \text{ N/m}$$

$$C_{34} = \frac{0.3 \times 6.895 \times 10^{10} \times (3.81)^3 \times 10^{-12}}{12\left[1 - (0.3)^2\right]} = 0.105 \text{ N-m}$$

REFERENCES

1. Rose, R. G.: Dynamics of the Atlas 5-CPS Longitudinal Oscillation Following Launch as Related to the Tank Pressure Regulation System. Rep. GDA63-0712 (Contracts AF 04(694)-196 and AF 04(694)-240), Gen. Dyn./Astronaut., Dec. 31, 1963. (Available from DDC as AD 435036.) Vol. I: Longitudinal Model Development. Vol. II: Pneumatic System Model Development.

2. Tai, C. L.; Loh, M. M. H.; and Kraft, L. E.: Evaluation Study of S-II Stage Longitudinal Oscillations (POGO). SID 66-1455 (Contract NAS7-200), N. Amer. Aviat., Inc., Sept. 30, 1966.

3. Pinson, Larry D.; and Leonard, H. Wayne: Longitudinal Vibration Characteristics of the 1/10-Scale Apollo/Saturn V Replica Model. NASA TN D-5159, 1969.

4. Pinson, Larry D.: Longitudinal Spring Constants for Liquid-Propellant Tanks with Ellipsoidal Ends. NASA TN D-2220, 1964.

5. Archer, J. S.; and Rubin, C. P.: Improved Analytic Longitudinal Response Analysis for Axisymmetric Launch Vehicles. Vol. I – Linear Analytic Model. NASA CR-345, 1965.

6. Rubin, C. P.; and Wang, T. T.: Improved Analytic Longitudinal Response Analysis for Axisymmetric Launch Vehicles. Vol. II – Computer Program Description. NASA CR-346, 1965.

7. Archer, J. S.; and Rubin, C. P.: Improved Linear Axisymmetric Shell-Fluid Model for Launch Vehicle Longitudinal Response Analysis. Matrix Methods in Structural Mechanics, AFFDL-TR-66-80, U.S. Air Force, Nov. 1966, pp. 823-847. (Available from DDC as AD 646 300.)

8. Thompson, William M., Jr.: An Investigation of the Response of a Scaled Model of a Liquid-Propellant Multistage Launch Vehicle to Longitudinal Excitation. NASA TN D-3975, 1967.

9. Pinson, Larry D.; Leonard, H. Wayne; and Raney, John P.: Analyses of the Longitudinal Dynamics of Launch Vehicles With Application to a 1/10-Scale Saturn V Model. J. Spacecraft Rockets, vol. 5, no. 3, Mar. 1968, pp. 303-308.

10. Leadbetter, Sumner A.; Leonard, H. Wayne; and Brock, E. John, Jr.: Design and Fabrication Considerations for a 1/10-Scale Replica Model of the Apollo/Saturn V. NASA TN D-4138, 1967.

11. Vehicle Dynamics Group: 1/10 Scale Saturn V Model Structural Dynamic Analysis. Doc. No. D5-15631 A (Contract No. NAS8-5608), Boeing Co., May 1, 1967.

12. Leadbetter, Sumner A., coordinator: Application of Analysis and Models to Structural Dynamic Problems Related to the Apollo-Saturn V Launch Vehicle. NASA TN D-5831, 1970.

TABLE I.- MASS AND STIFFNESS DATA FOR THE SPRING-MASS ANALYSIS[a]

Mass name (b)	Index for mass or spring constant (c)	Station, m	Mass, kg	Spring constant, N/m
LES	1	10.688	1.978	0.2477×10^8
LES—CM	2	9.754	3.486	1.8514
CM—SM	3	9.599	12.71	.1198
SM—SLA	4	9.130	11.68	.0898
SLA	5	8.450	.6754	.0226
LM	6	8.450	2.992	.0170
LM	7	8.450	8.987	.7215
SLA—IU—S-IVB forward skirt	8	8.277	1.851	.1820
S-IVB forward skirt—fuel tank	9	7.875	3.715	.6658
S-IVB fuel tank—lox tank—aft skirt	10	7.193	4.335	.1133
S-IVB engine	11	6.721	1.469	.1697
S-IVB lox	12	7.193	79.40	.3285
S-IVB liquid hydrogen	13	6.758	18.37	.9103
S-IVB aft skirt—interstage adapter	14	6.976	4.201	2.5367
Interstage adapter—S-II forward skirt	15	6.398	4.341	.4583
S-II forward skirt—fuel tank	16	6.063	10.29	2.2689
S-II fuel tank—lox tank—aft skirt	17	4.694	12.98	.6051
S-II aft skirt—interstage adapter	18	4.539	16.16	.1123
S-II outer engine	19	4.227	5.945	.2075
S-II center engine	20	4.227	1.942	.6858
S-II lox	21	4.694	349.1	8.9129
S-II liquid hydrogen	22	5.379	71.08	2.2006
S-IC forward skirt—lox tank	23	3.559	23.90	.0319
S-IC lox tank—intertank adapter	24	2.317	19.56	1.2262
Intertank adapter—S-IC fuel tank	25	1.529	16.16	1.0791
S-IC fuel tank—aft skirt	26	.927	31.24	.1765
S-IC aft skirt—engines	27	.285	71.24	.4819
S-IC fuel	28	1.050	583.1	1.5033
S-IC lox	29	2.938	1342	2.1113
	30			1.3620
	31			.8585
	32			5.5599

[a]The values shown in this table apply to the 100-percent-weight condition. In the 50-percent-weight condition, $m_{28} = 291.6$ kg, $m_{29} = 671.0$ kg, $k_{25} = 1.1122 \times 10^8$ N/m, $k_{26} = 0.1058 \times 10^8$ N/m, $k_{27} = 1.0508 \times 10^8$ N/m, $k_{29} = 2.2105 \times 10^8$ N/m, $k_{30} = 0.0189 \times 10^8$ N/m, and $k_{31} = 0.9751 \times 10^8$ N/m. In the empty condition, $m_{28} = m_{29} = 0$, $k_{25} = 1.2084 \times 10^8$ N/m, $k_{29} = 2.2288 \times 10^8$ N/m, and $k_{26} = k_{27} = k_{30} = k_{31} = 0$.

[b]Definition of mass-name abbreviations may be found in figure 4.

[c]See figure 6.

TABLE II.- ORTHOTROPIC SHELL ELASTIC CONSTANTS FOR 1/10-SCALE SATURN V MODEL[a]

Model component	Shell no. (b)	C_{11}, N/m	C_{12}, N/m	C_{22}, N/m	C_{33}, N-m	C_{34}, N-m	C_{44}, N-m
Launch escape system	1	9.174×10^7	2.752×10^7	9.174×10^7	11.229	3.369	11.229
Command module	2	10.584×10^7	3.175×10^7	10.584×10^7	0.002	0.001	0.002
		.520	.156	.520	.640	.191	.640
					5.102	1.528	5.102
					17.215	5.154	17.215
Service module	3	0.520×10^7	0.156×10^7	0.520×10^7	0.002	0.001	0.002
Spacecraft lunar module adapter, forward section	4	0.654×10^7	0.196×10^7	0.654×10^7	56.527	16.959	56.527
					33.860	10.158	33.860
					25.510	7.653	25.510
					24.317	7.295	24.317
Spacecraft lunar module adapter, aft section	5	0.654×10^7	0.196×10^7	0.654×10^7	66.870	20.061	66.870
					59.591	17.877	59.591
					56.910	17.073	56.910
					56.527	16.959	56.527
Instrument unit and S-IVB forward skirt	6	1.085×10^7	0.296×10^7	0.891×10^7	79.259	18.608	44.794
S-IVB forward bulkhead	-7	1.347×10^7	0.404×10^7	1.347×10^7	0.035	0.011	0.035
S-IVB LH_2 tank	8	2.627×10^7	0.751×10^7	2.627×10^7	1.302	0.068	1.302
Common bulkhead	-9	1.924×10^7	0.577×10^7	1.924×10^7	107.57	32.273	107.57
Aft bulkhead	-10	2.309×10^7	0.693×10^7	2.309×10^7	0.179	0.054	0.179
Aft skirt	11	2.687×10^7	0.231×10^7	2.372×10^7	44.007	0.002	576.57
S-IVB/S-II adapter	12	2.420×10^7	0.231×10^7	2.063×10^7	3 374.0	0.002	4 688.6
Forward skirt	13	3.357×10^7	0.693×10^7	3.264×10^7	49.298	0.054	616.47
		2.291	.559	1.725	42.337	.017	
					39.772	.004	
					39.411	.002	
Forward bulkhead	-14	3.849×10^7	1.155×10^7	3.849×10^7	0.828	0.248	0.828
LH_2 tank	15	3.174×10^7	0.866×10^7	3.166×10^7	13.772	0.105	309.77
Common bulkhead	-16	4.619×10^7	1.386×10^7	4.619×10^7	1 716.4	514.90	1 716.4
Aft bulkhead	-17	3.849×10^7	1.155×10^7	3.849×10^7	0.828	0.248	0.828
Aft skirt	18	4.194×10^7	0.404×10^7	2.239×10^7	168.58	0.011	1 419.2
S-II/S-IC adapter	19	3.877×10^7	0.404×10^7	2.269×10^7	164.51	0.011	121 066
Lox forward bulkhead	-20	4.811×10^7	0.722×10^7	4.811×10^7	1.616	0.242	1.616
Lox tank	21	5.658×10^7	1.443×10^7	5.451×10^7	115.59	0.485	6 161.2
		4.503	1.097	4.296			
Lox aft bulkhead	22	5.388×10^7	1.617×10^7	5.388×10^7	2.271	0.678	2.278
Intertank	23	3.746×10^7	0.002×10^7	0.771×10^7	640.4	0.127	0.076
Fuel forward bulkhead	-24	3.849×10^7	1.155×10^7	3.849×10^7	0.825	0.249	0.825
Fuel tank	25	4.696×10^7	1.097×10^7	5.049×10^7	134.1	0.213	17 822
		4.311	.981	4.665			
Fuel aft bulkhead	-26	4.234×10^7	1.270×10^7	4.234×10^7	1.107	0.328	1.107
Aft skirt	27	11.617×10^7	1.847×10^7	11.018×10^7	19 316	1.017	94 188
Filler cylinder, S-IVB	28	2.627×10^7	0.788×10^7	2.627×10^7	1.302	0.391	1.302
Filler cylinder, S-II	29	3.202×10^7	0.959×10^7	3.202×10^7	13.423	48.473	309.48

[a]Where more than one value is given for a quantity, the first value corresponds to the aft end of the shell.

[b]Shell location as shown in figure 5.

TABLE III.- SUMMARY OF MEASURED AND CALCULATED LONGITUDINAL NATURAL FREQUENCIES FOR THE 1/10-SCALE SATURN V MODEL

Figure	Mode description	Natural frequencies, Hz, for –									
		100-percent-weight condition				50-percent-weight condition			Empty condition		
		Experiment (a)	Finite element	Spring mass	Spring mass (equivalent) (b)	Experiment	Finite element	Spring mass	Experiment	Finite element	Spring mass
13	First S-IC lox										
	With joint effects	30.9	33.2	38.0	34.9	71.2	74.9	62.8			
	Without joint effects		33.6	39.0	34.9		74.9	62.8			
14	S-II fuel										
	With joint effects		39.1				39.1			39.1	
	Without joint effects		39.2				39.2			39.2	
15	First structural										
	With joint effects	40.2	43.9	41.2	37.3	42.0	43.2	42.0	51.1	49.4	48.8
	Without joint effects		45.8	41.7	38.6		46.4	44.4		57.1	56.2
16	S-IVB fuel										
	With joint effects		51.3				51.4			51.6	
	Without joint effects		51.5				51.5			51.5	
17	Second structural										
	With joint effects	56.4	54.8	52.3	51.8	57.1	58.3	53.4	86.0	79.1	72.1
	Without joint effects		60.0	57.9	57.7		62.4	58.2		88.4	78.4
18	LM										
	With joint effects	71.3	69.5	69.2	69.0	71.2	69.7	69.2	69.6	69.5	69.2
	Without joint effects		72.1	71.0	70.8		72.7	71.0		71.9	71.0
19	Third structural										
	With joint effects		79.1	72.1	71.9		80.3	72.1		89.1	78.7
	Without joint effects		91.0	81.7	81.3		90.9	81.8		91.1	82.3
20	Second S-IC lox										
	With joint effects		84.6								
	Without joint effects		83.7								

[a]From reference 3.

[b]These values are results of the spring-mass analysis in which the liquid masses have been changed by the procedure discussed in references 3 and 9.

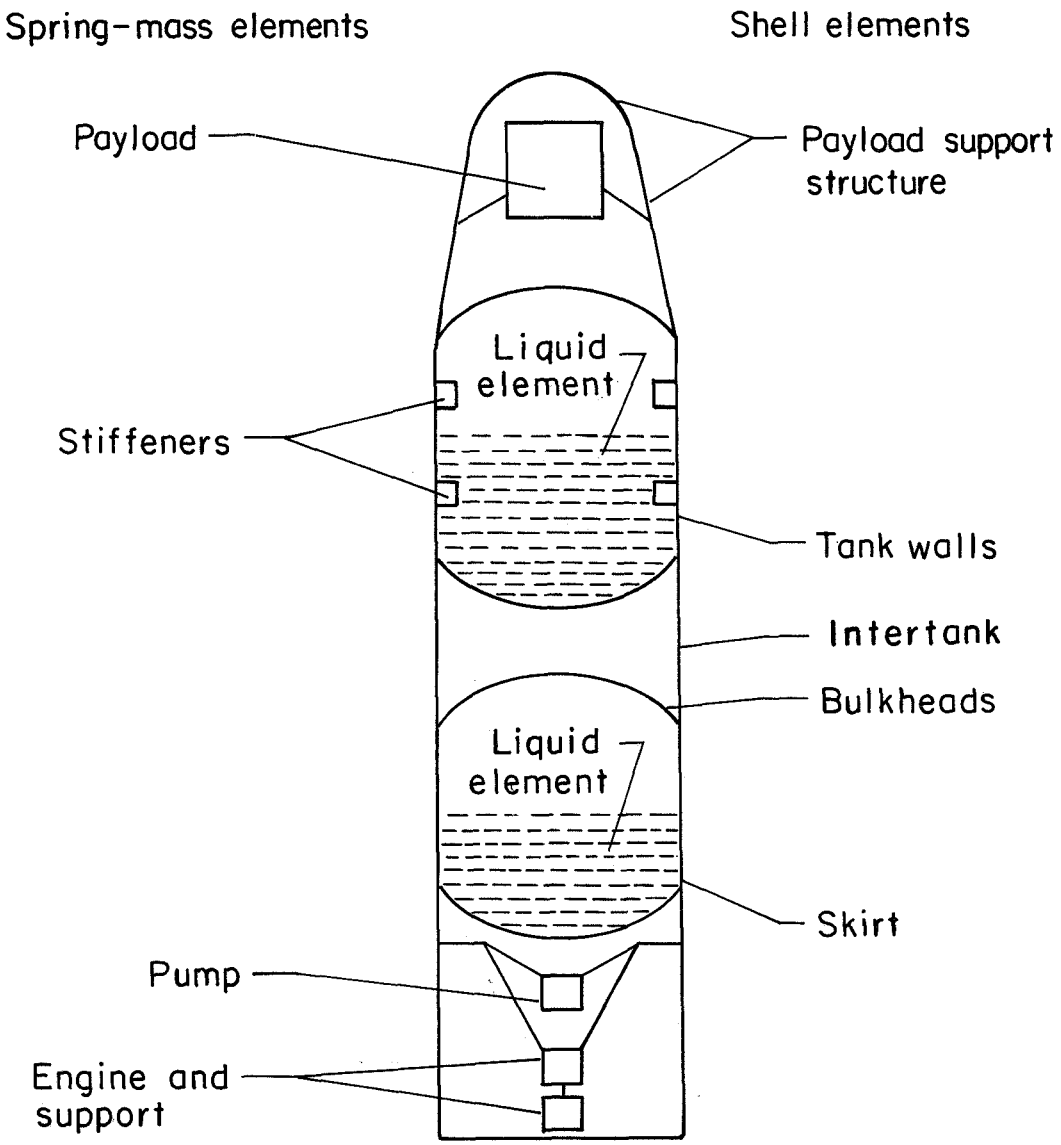

Figure 1.- Illustrative finite-element model.

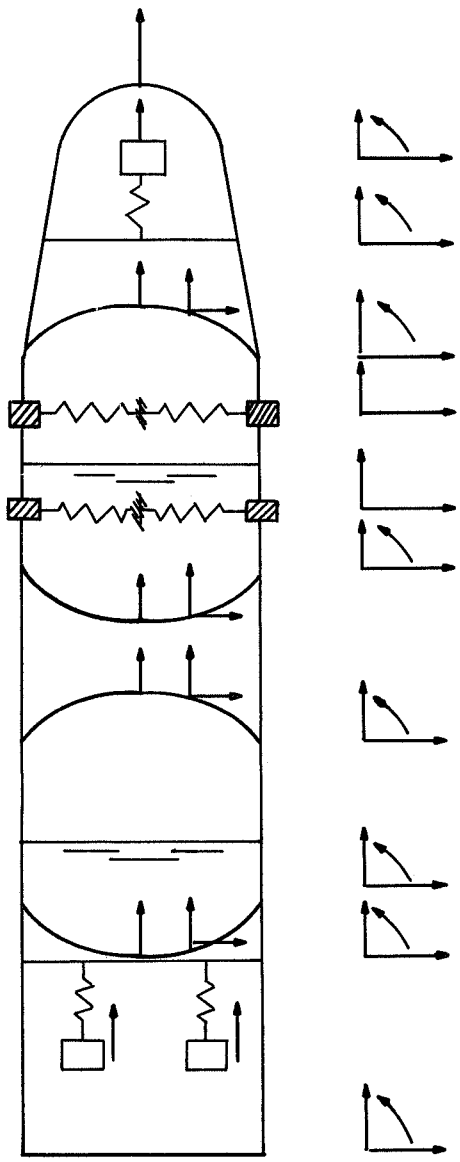

Figure 2.- Coordinate system for illustrative finite-element model.

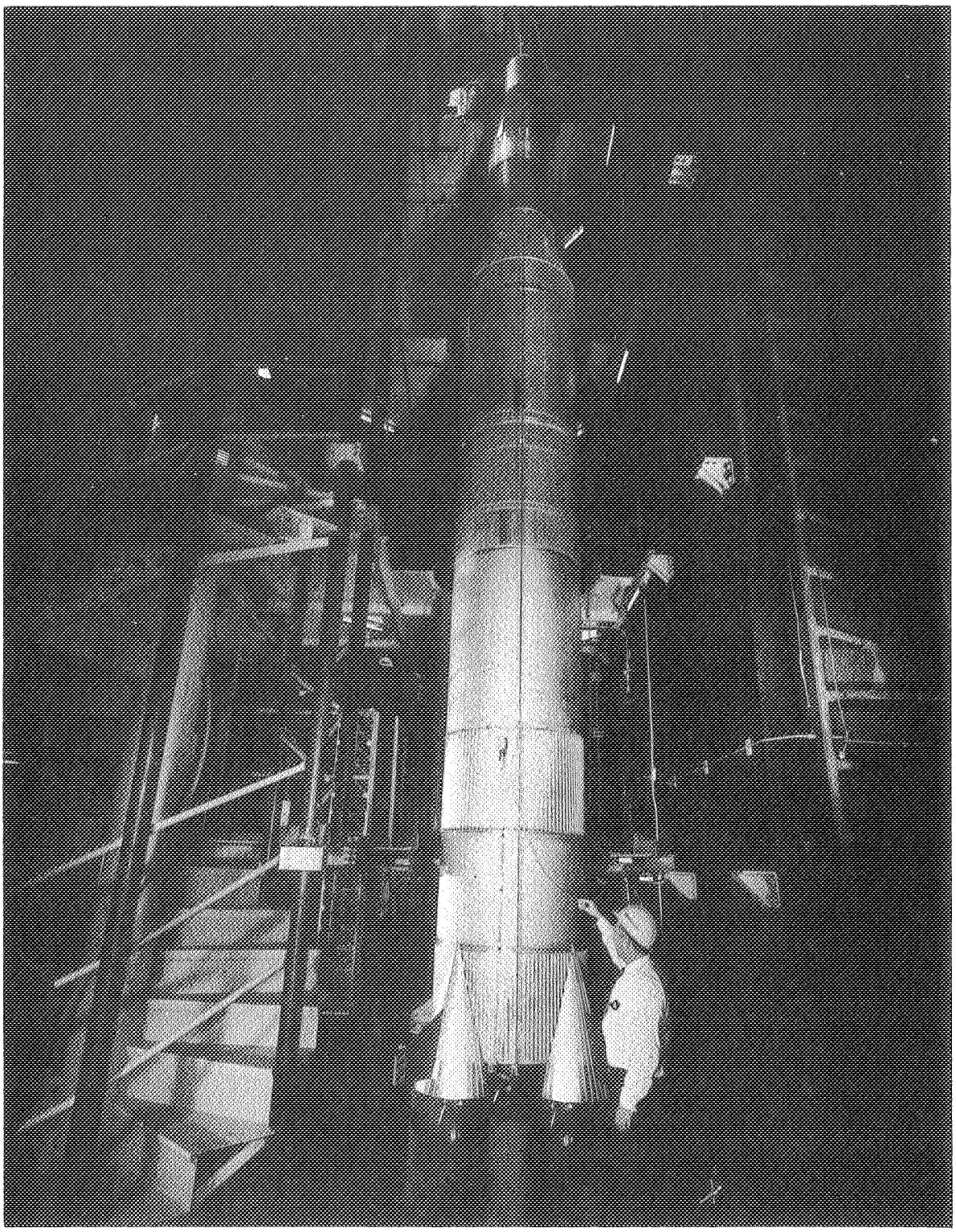

Figure 3.- Photograph of 1/10-scale model of Apollo/Saturn V launch vehicle. L-65-201

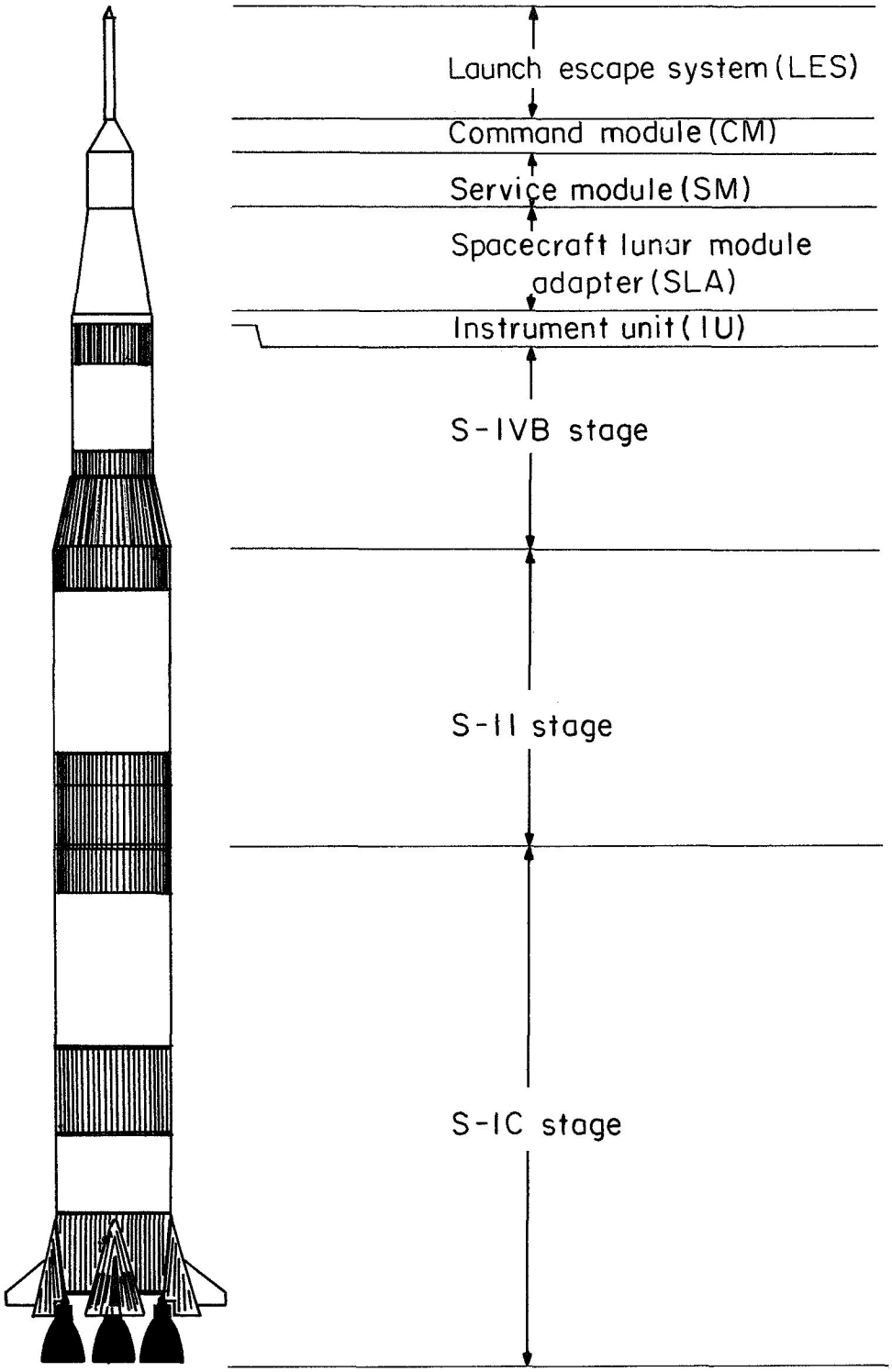

Figure 4.- Nomenclature for Apollo/Saturn V launch vehicle.

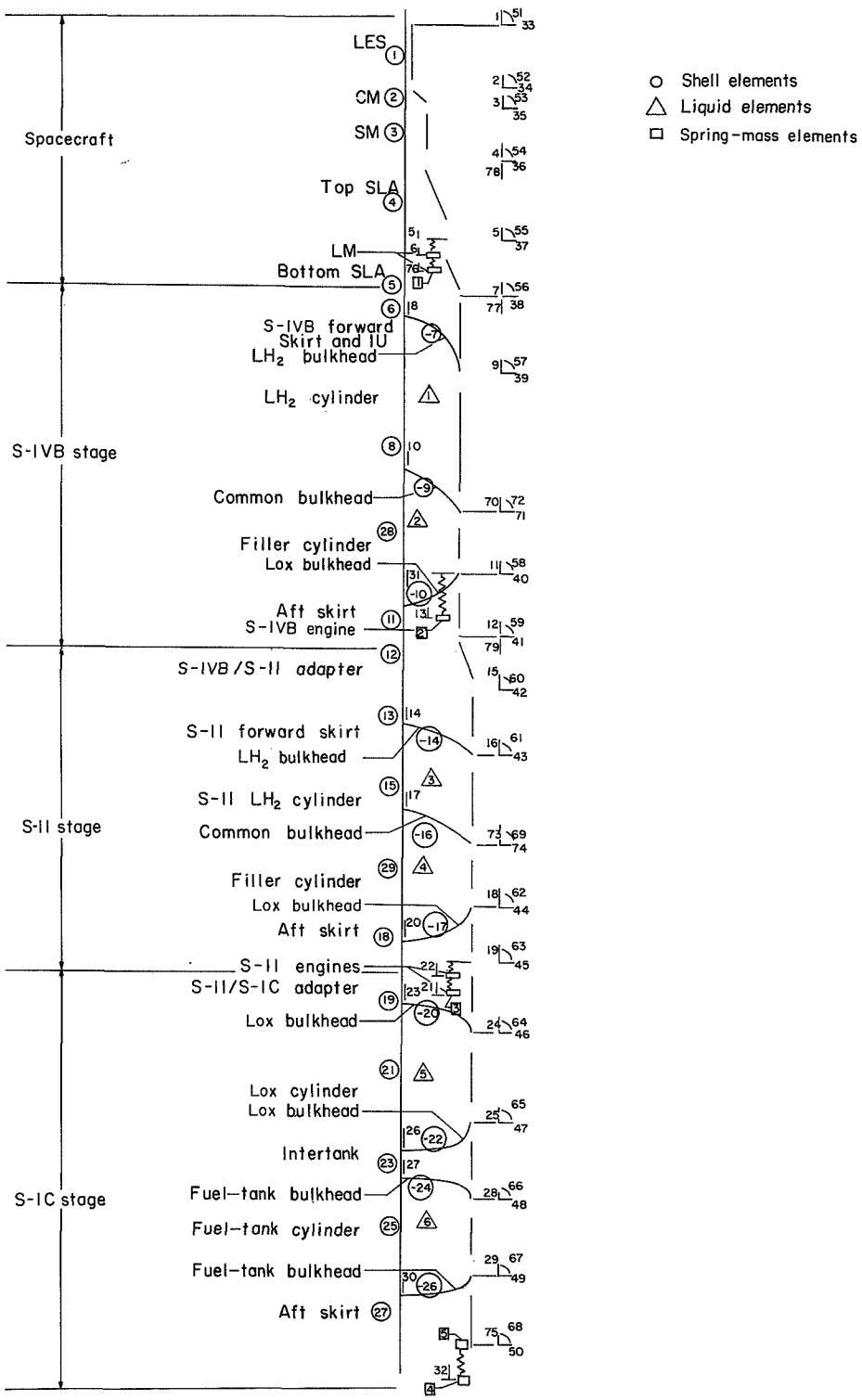

Figure 5.- Idealization of 1/10-scale Saturn V model for finite-element analysis.

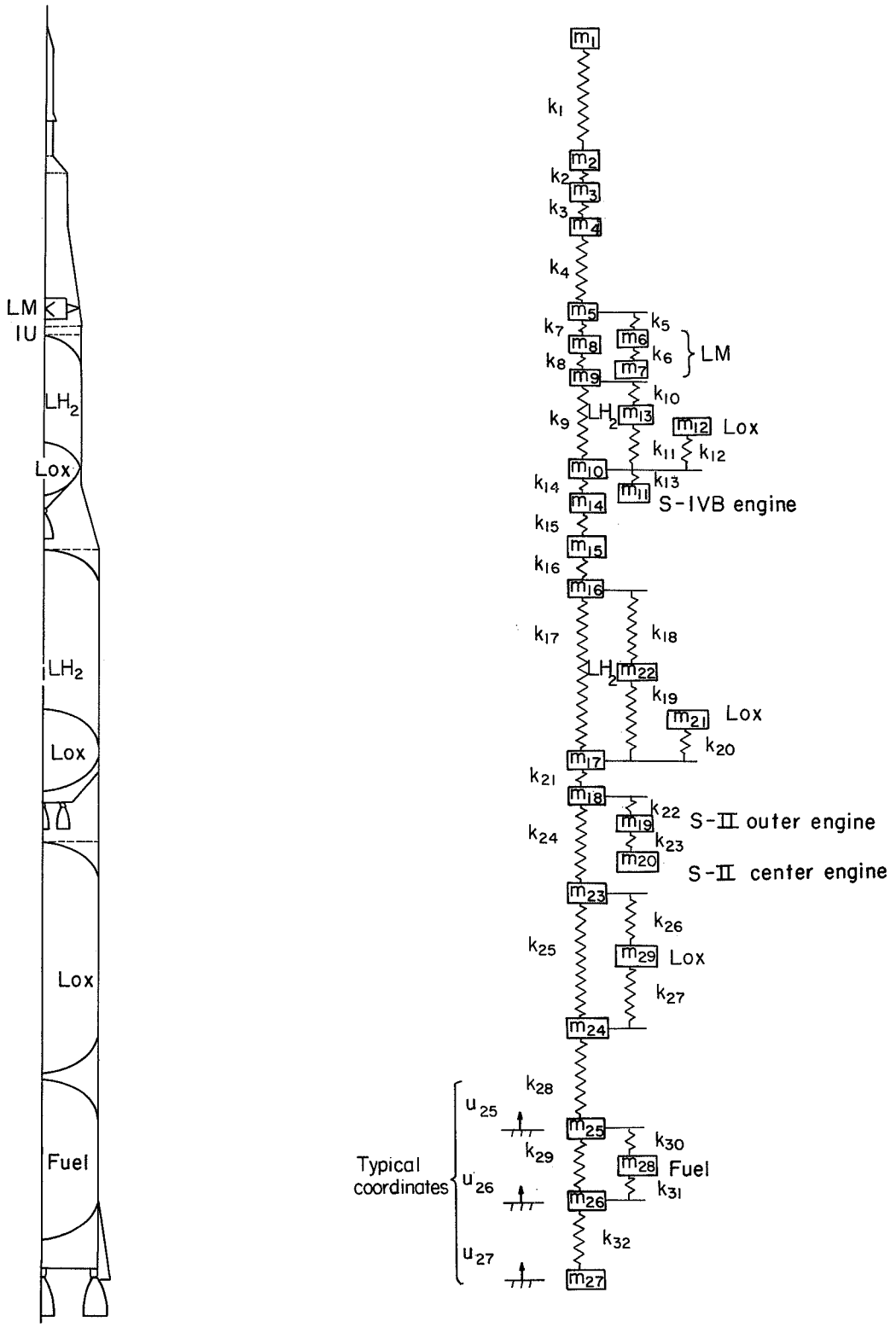

Figure 6.- Analytical model for spring-mass analysis.

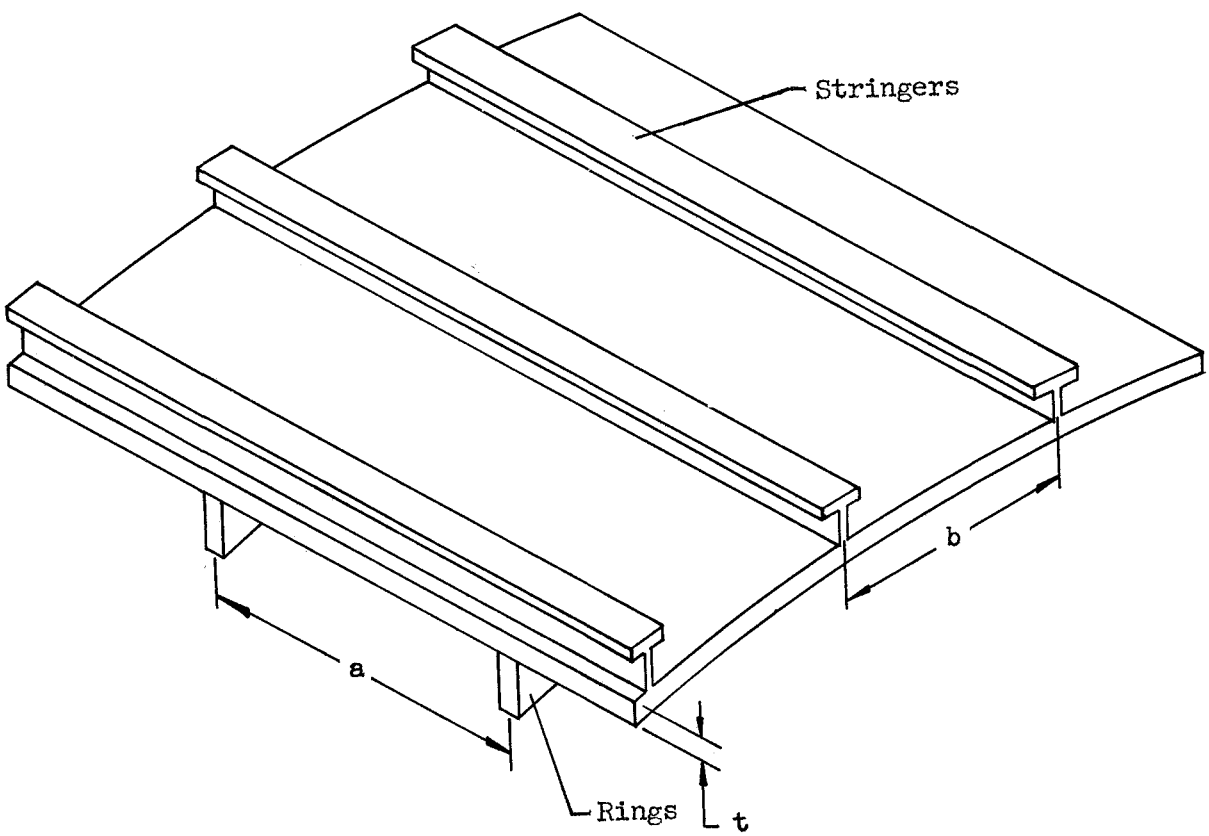

Figure 7.- Repeating element of a typical stiffened shell.

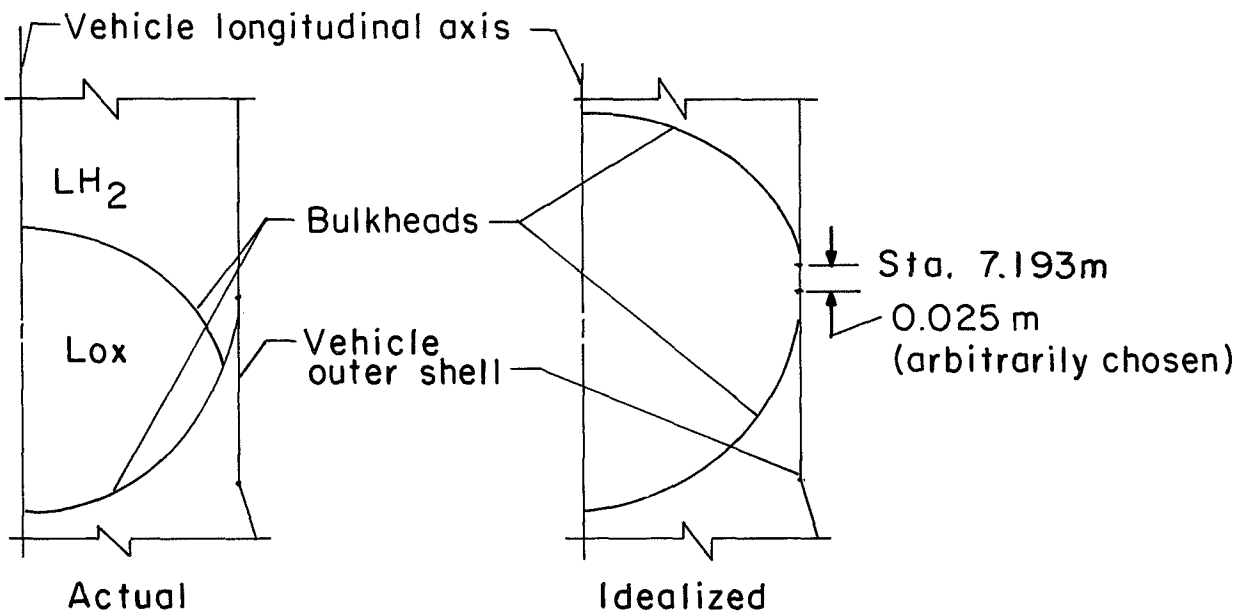

(a) Liquid oxygen tank of S-IVB stage.

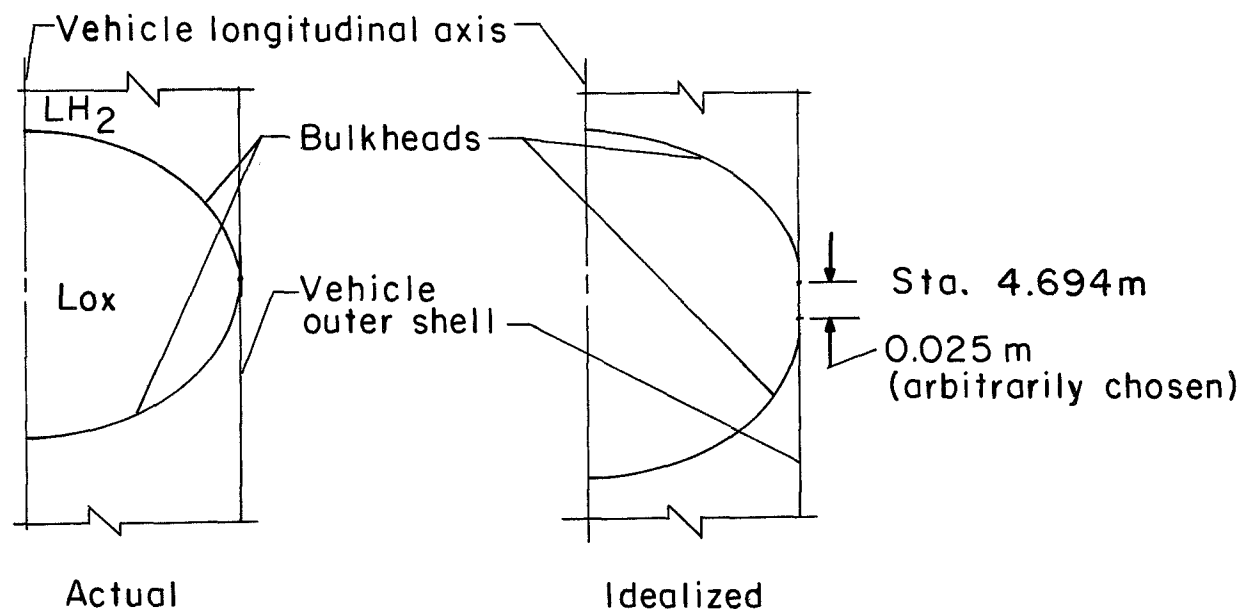

(b) Liquid oxygen tank of S-II stage.

Figure 8.- Liquid oxygen tanks of the S-IVB and S-II stages and their idealizations.

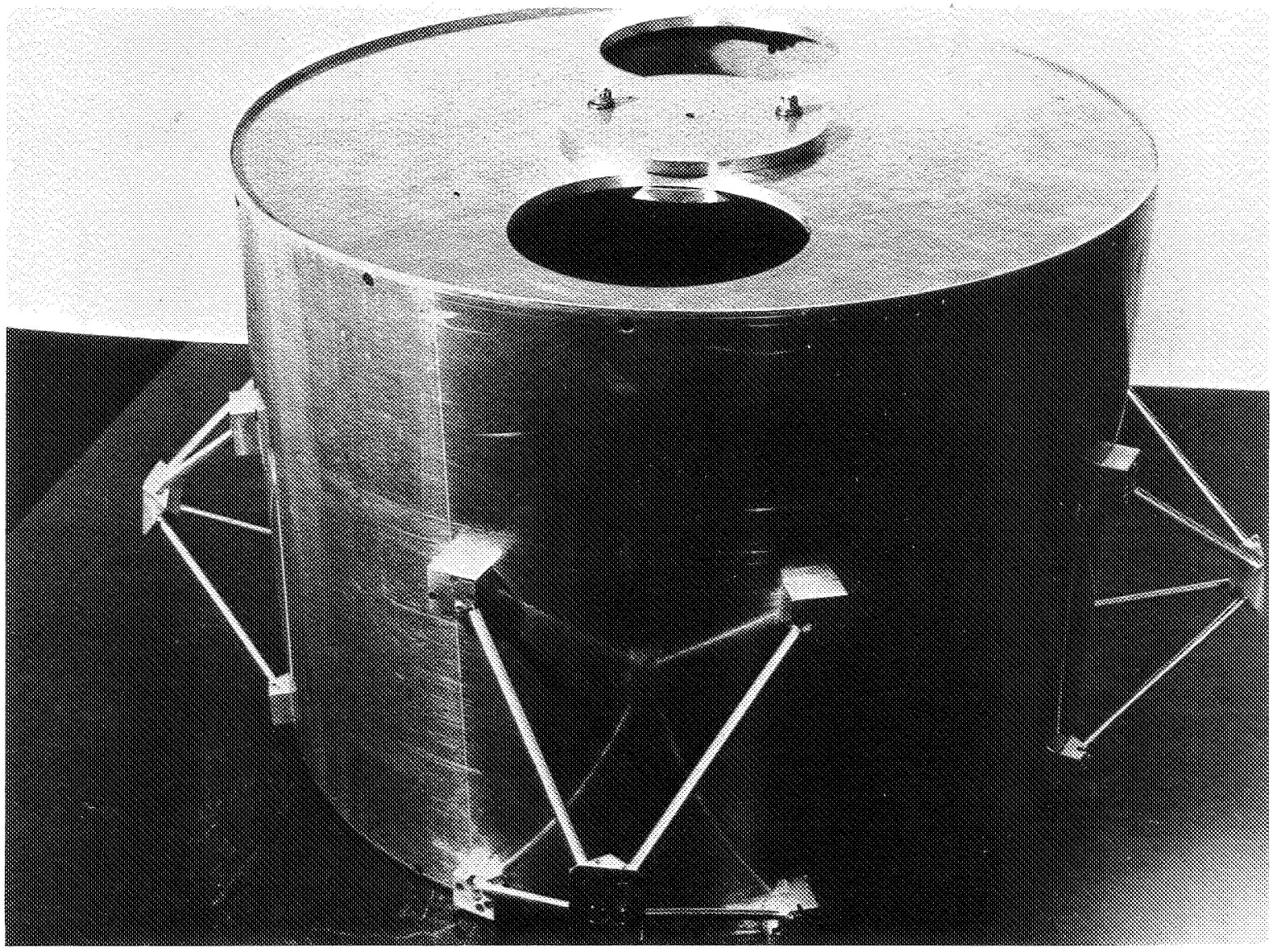

Figure 9.- Simulated lunar module.

L-70-1553

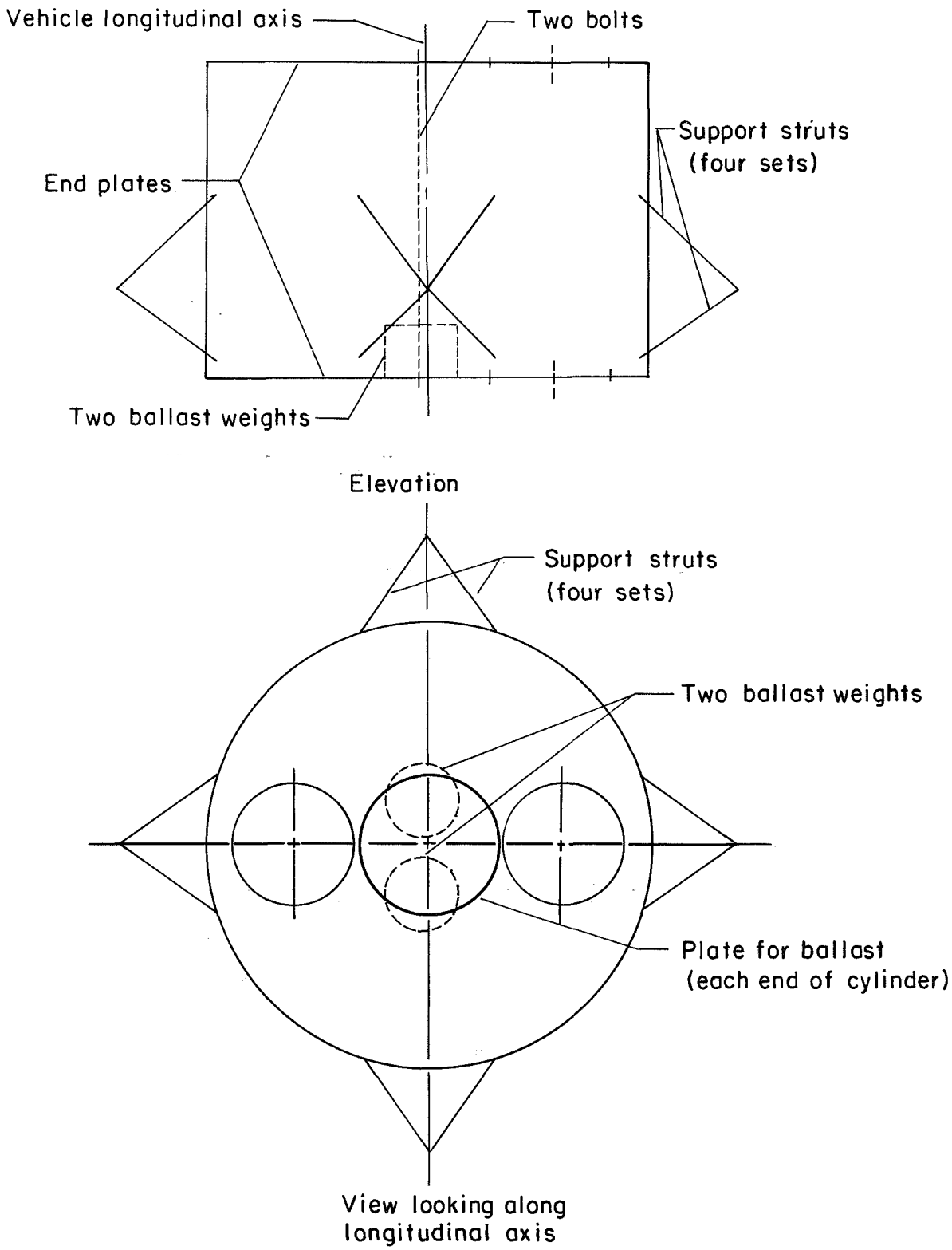

Figure 10.- Diagram of simulated lunar module.

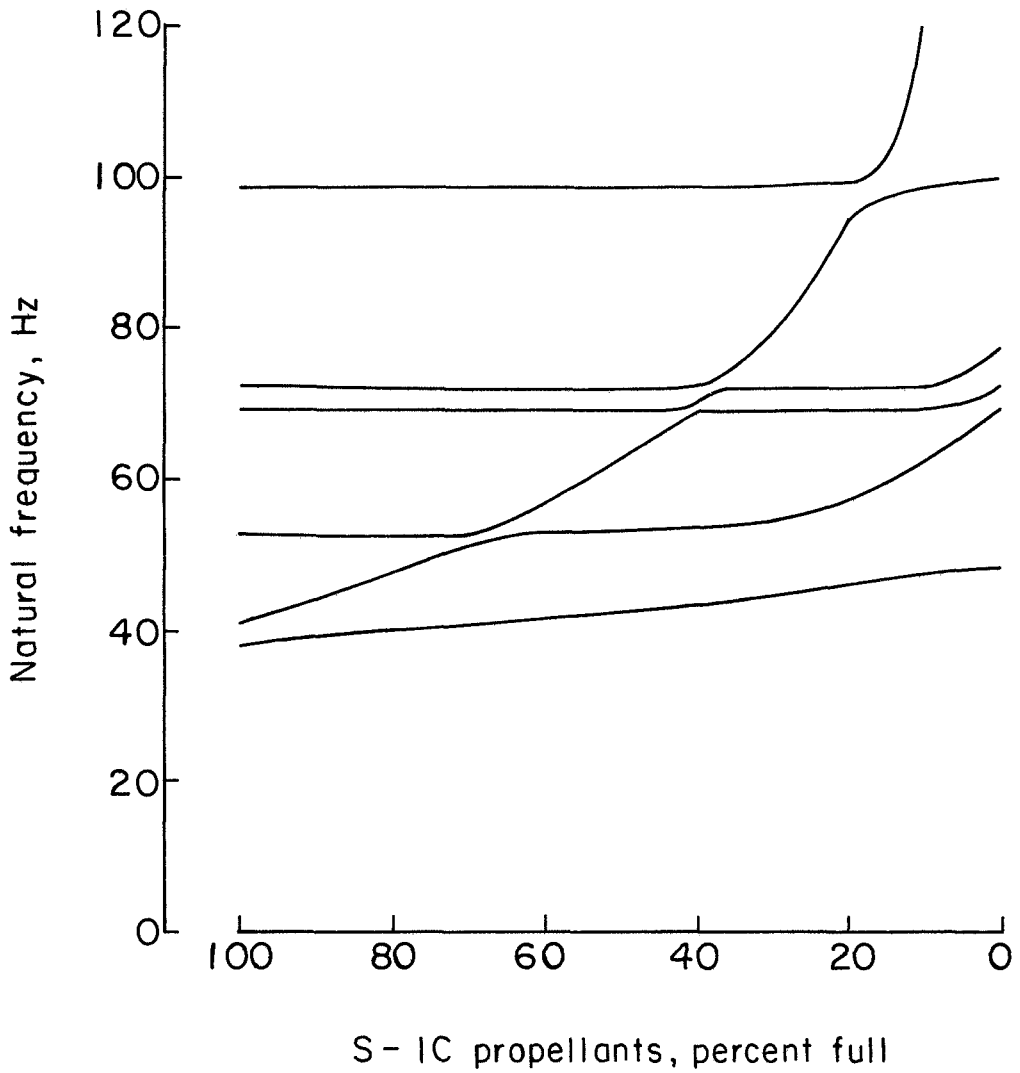

Figure 11.- Variation of natural frequencies predicted by the spring-mass analysis (joint effects included) with S-IC stage propellant loading.

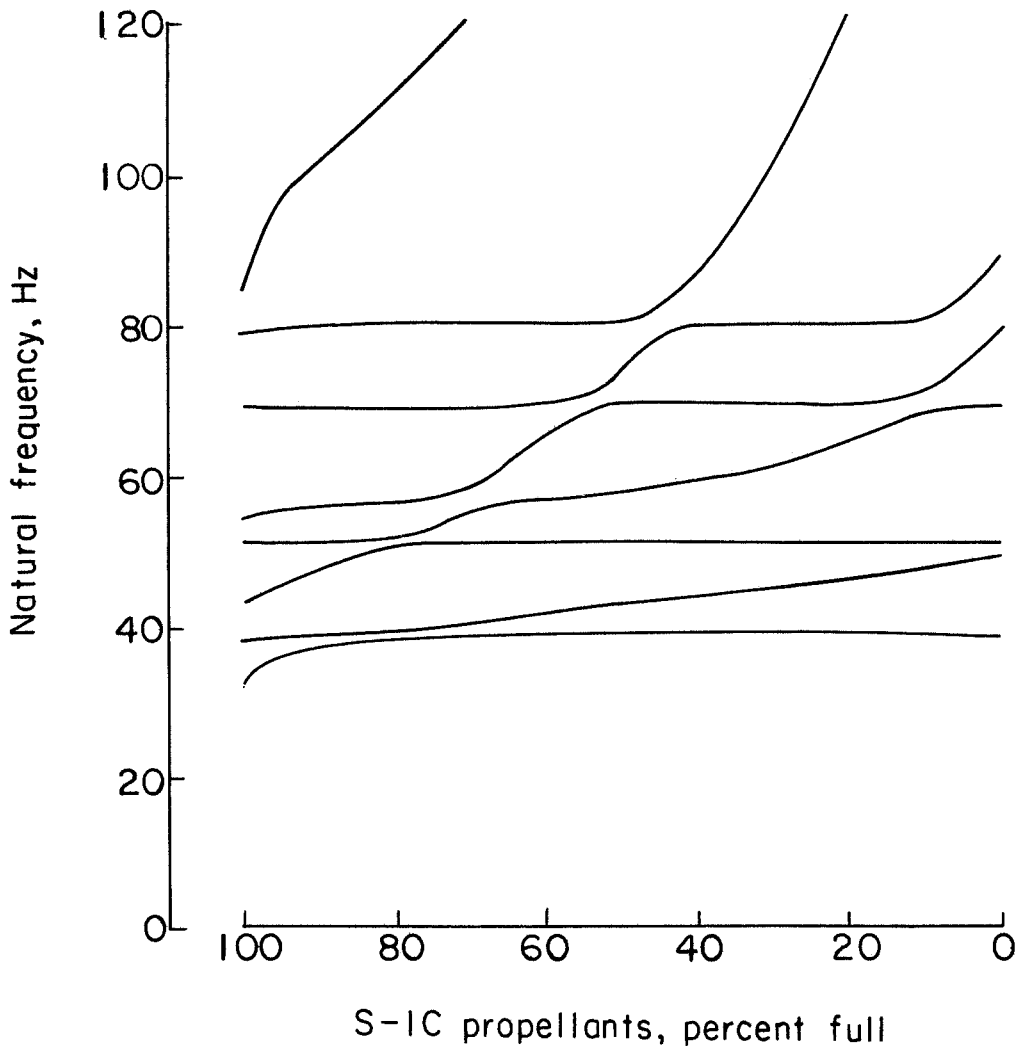

Figure 12.- Variation of natural frequencies predicted by the finite-element analysis (joint effects included) with S-IC stage propellant loading.

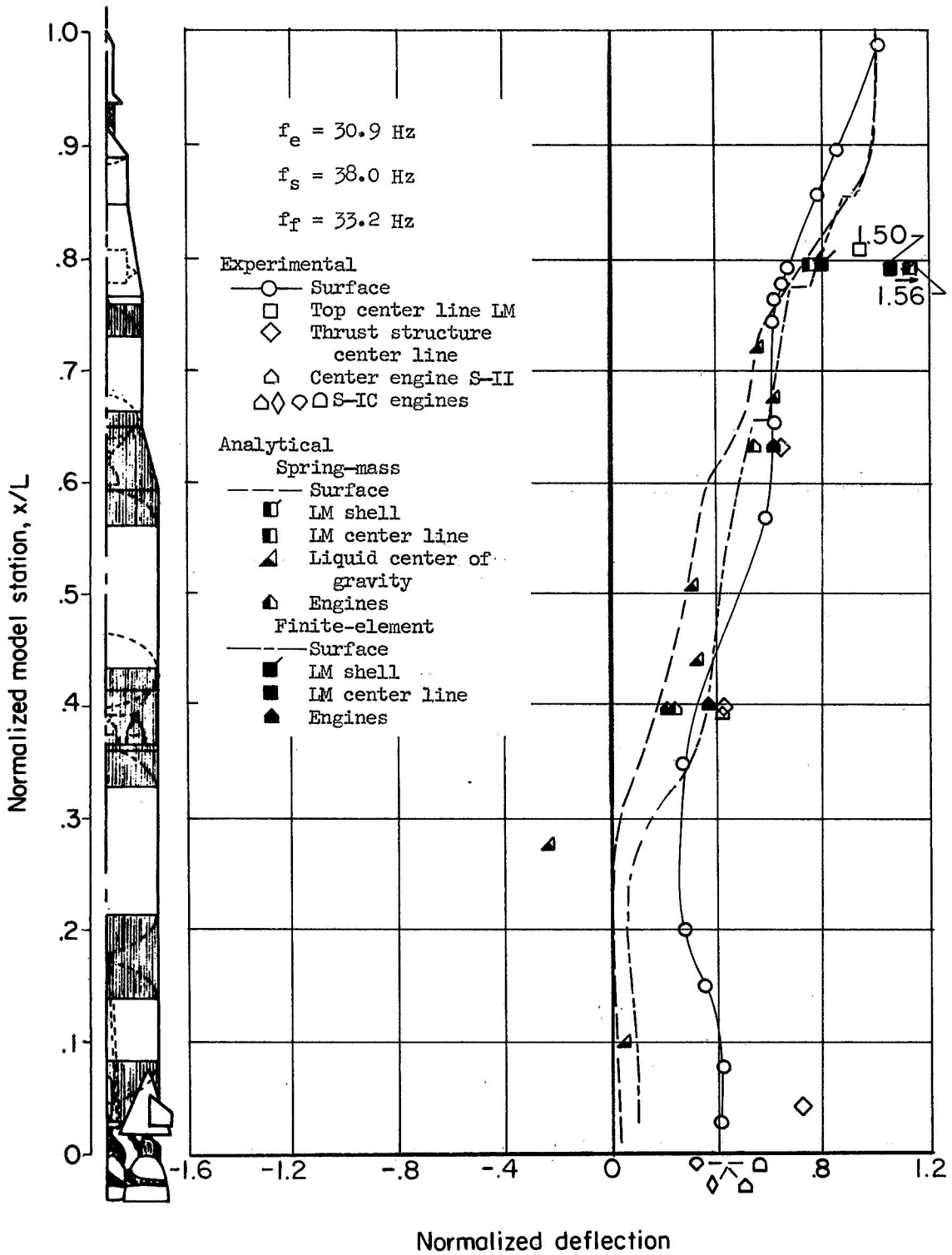

(a) 100-percent-weight condition.

Figure 13.- Experimental and analytical natural frequencies and mode shapes for first S-IC lox mode.

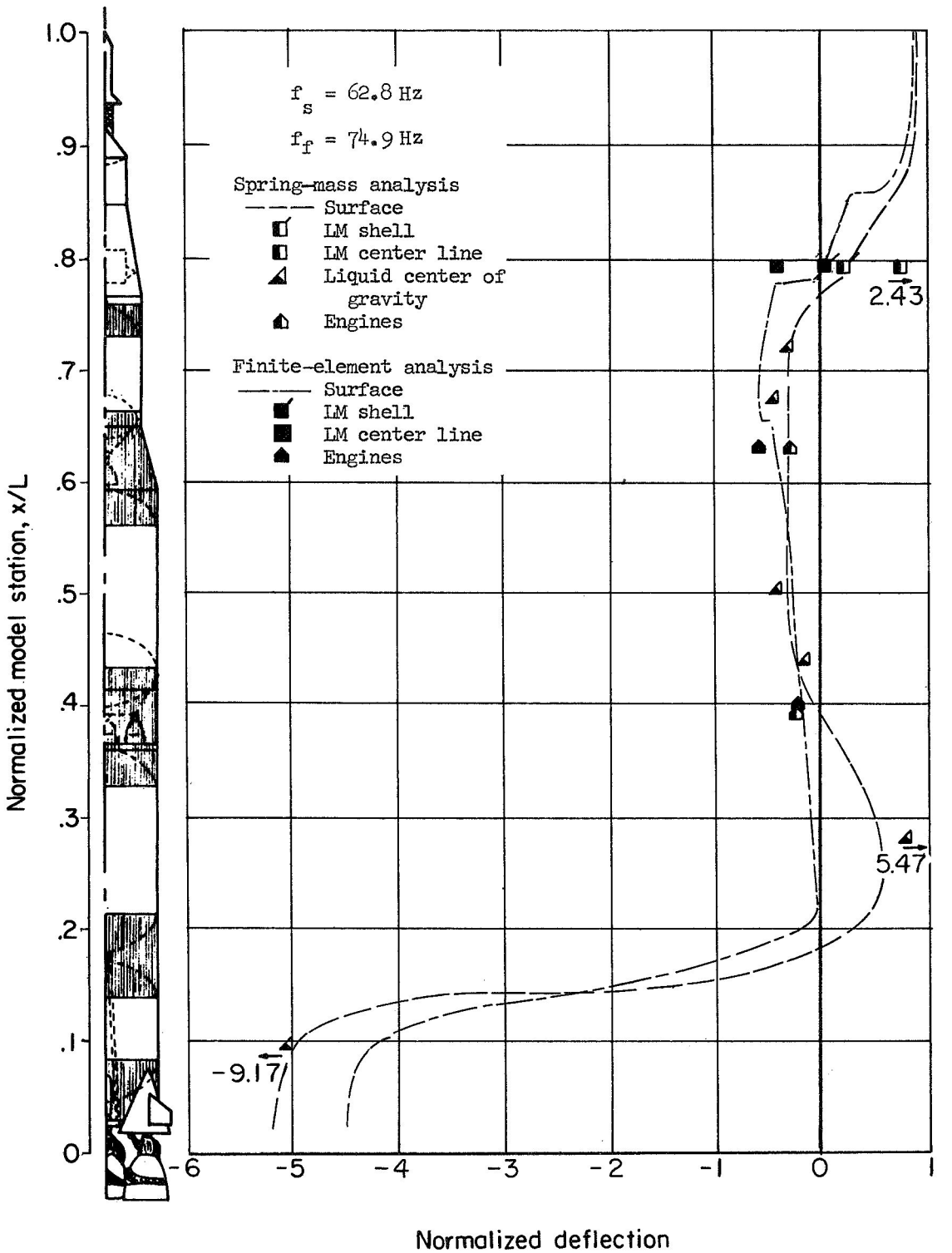

(b) 50-percent-weight condition.

Figure 13.- Concluded.

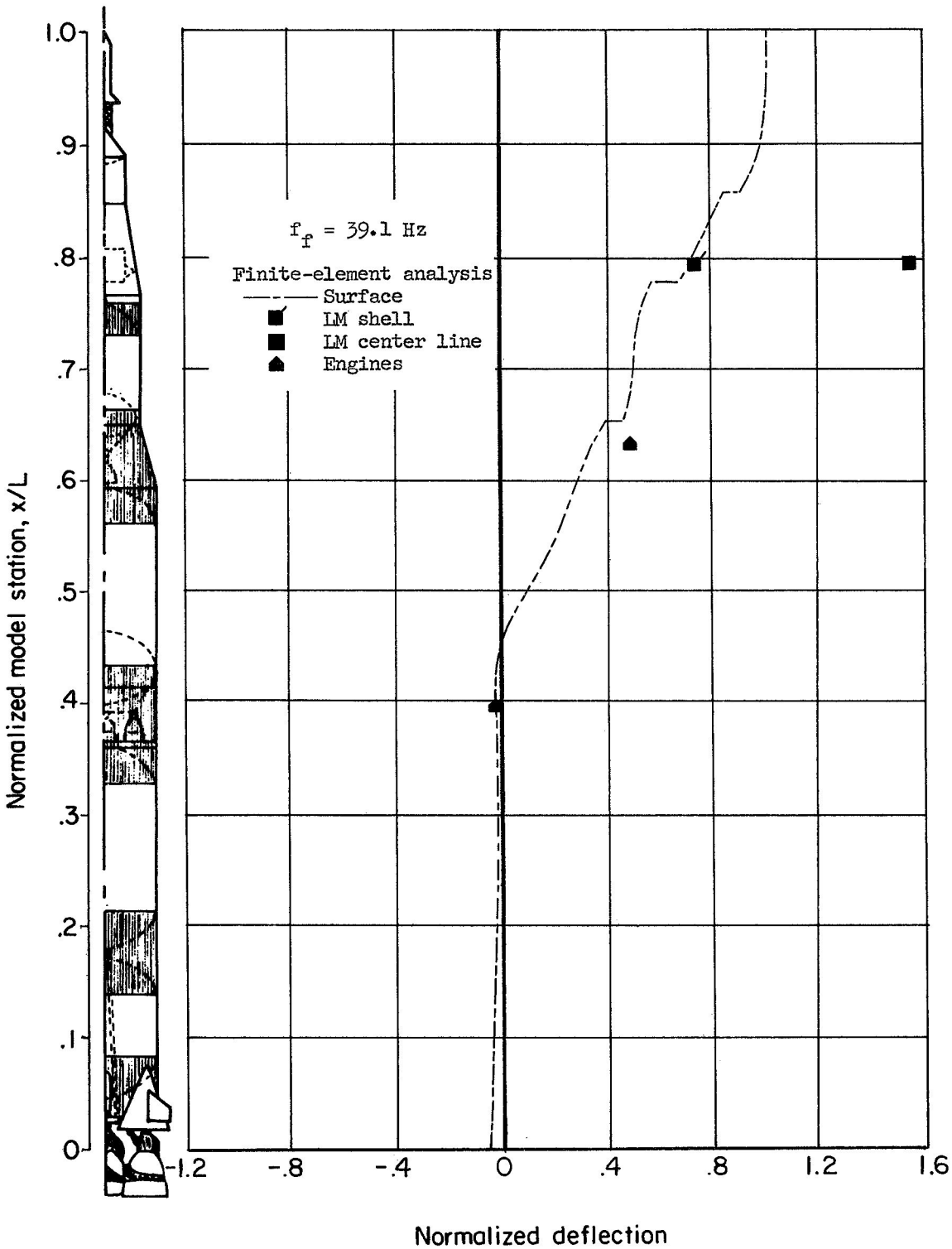

(a) 100-percent-weight condition.

Figure 14.- Natural frequencies and mode shapes for S-II fuel mode from finite-element analysis.

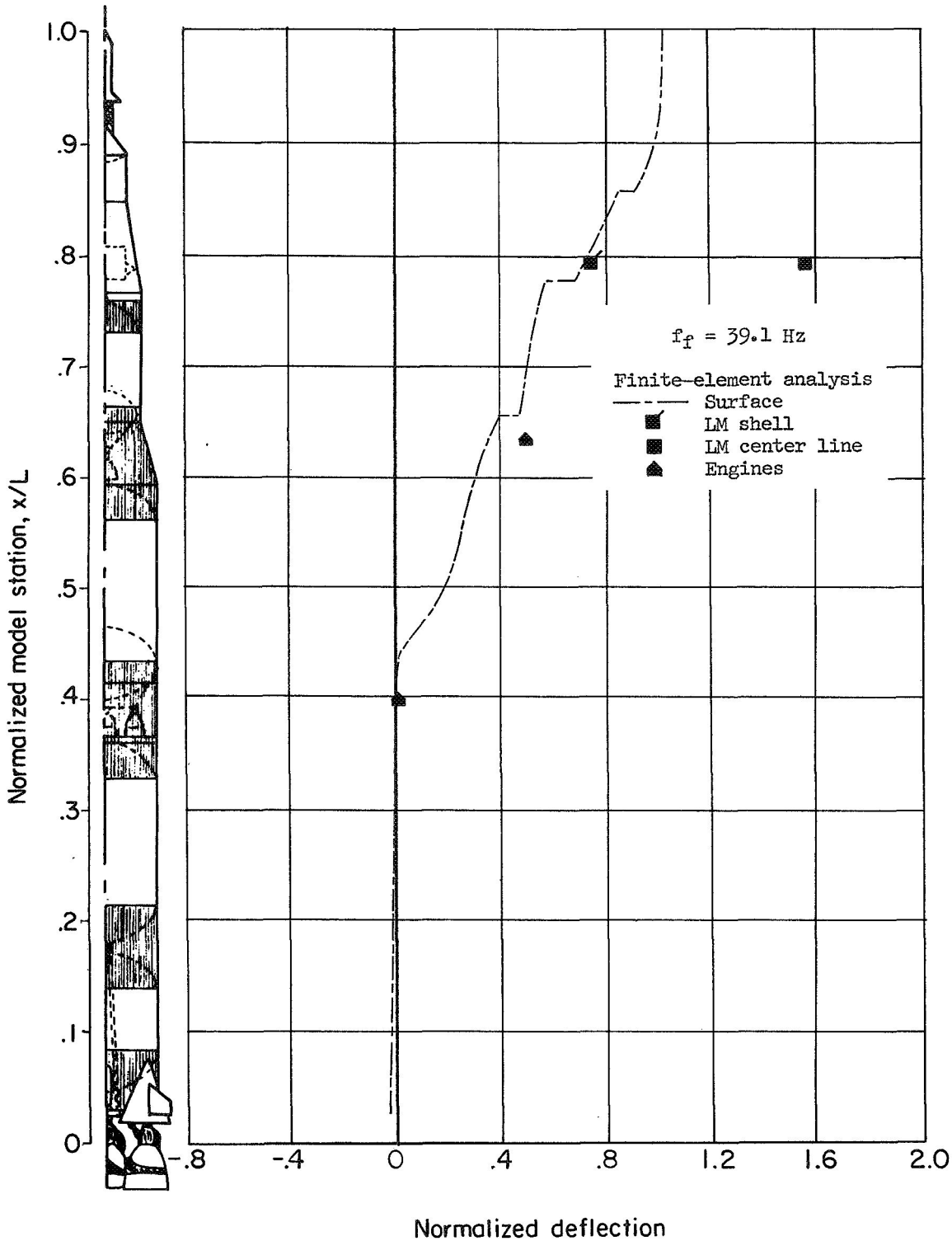

(b) 50-percent-weight condition.

Figure 14.- Continued.

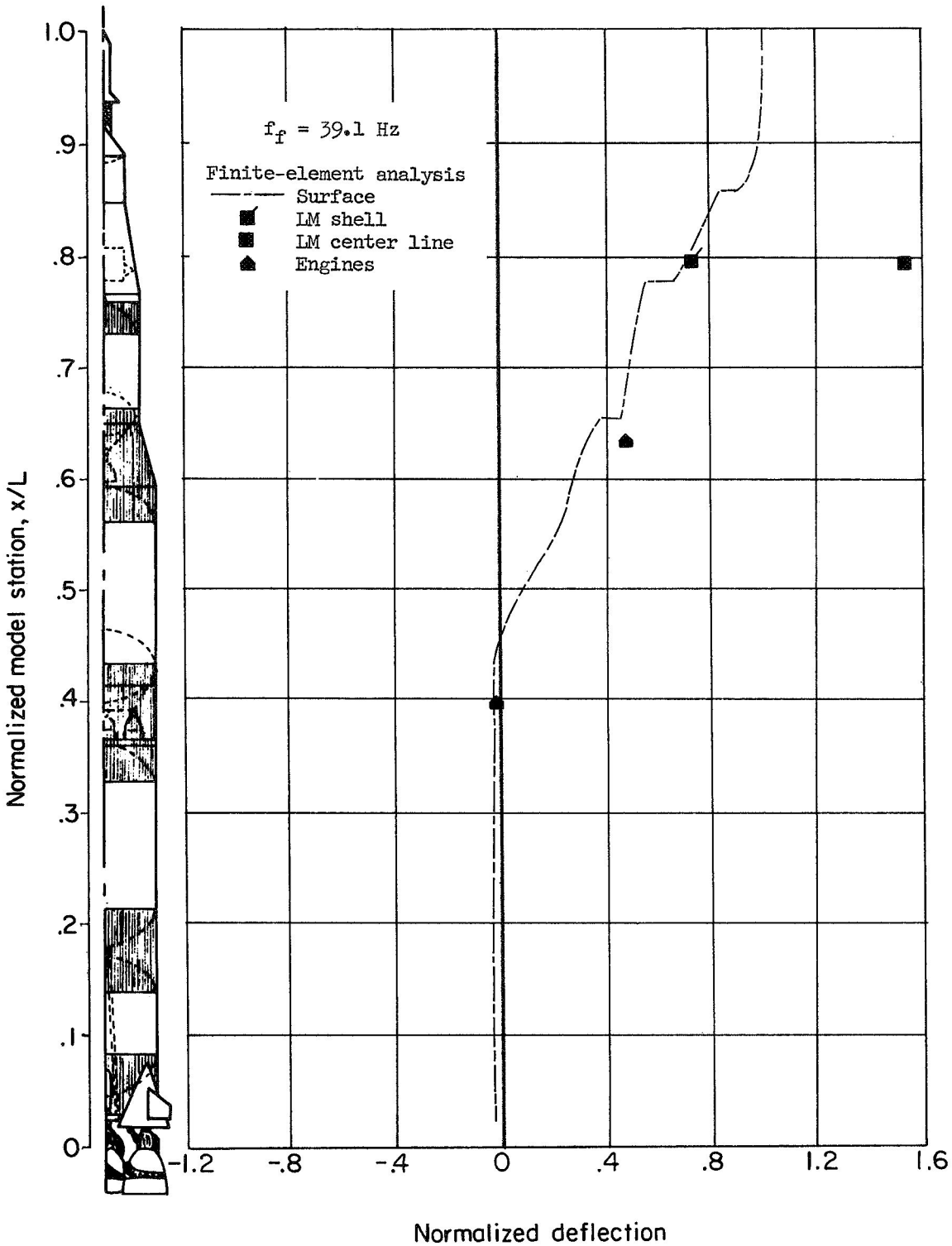

(c) Empty condition.

Figure 14.- Concluded.

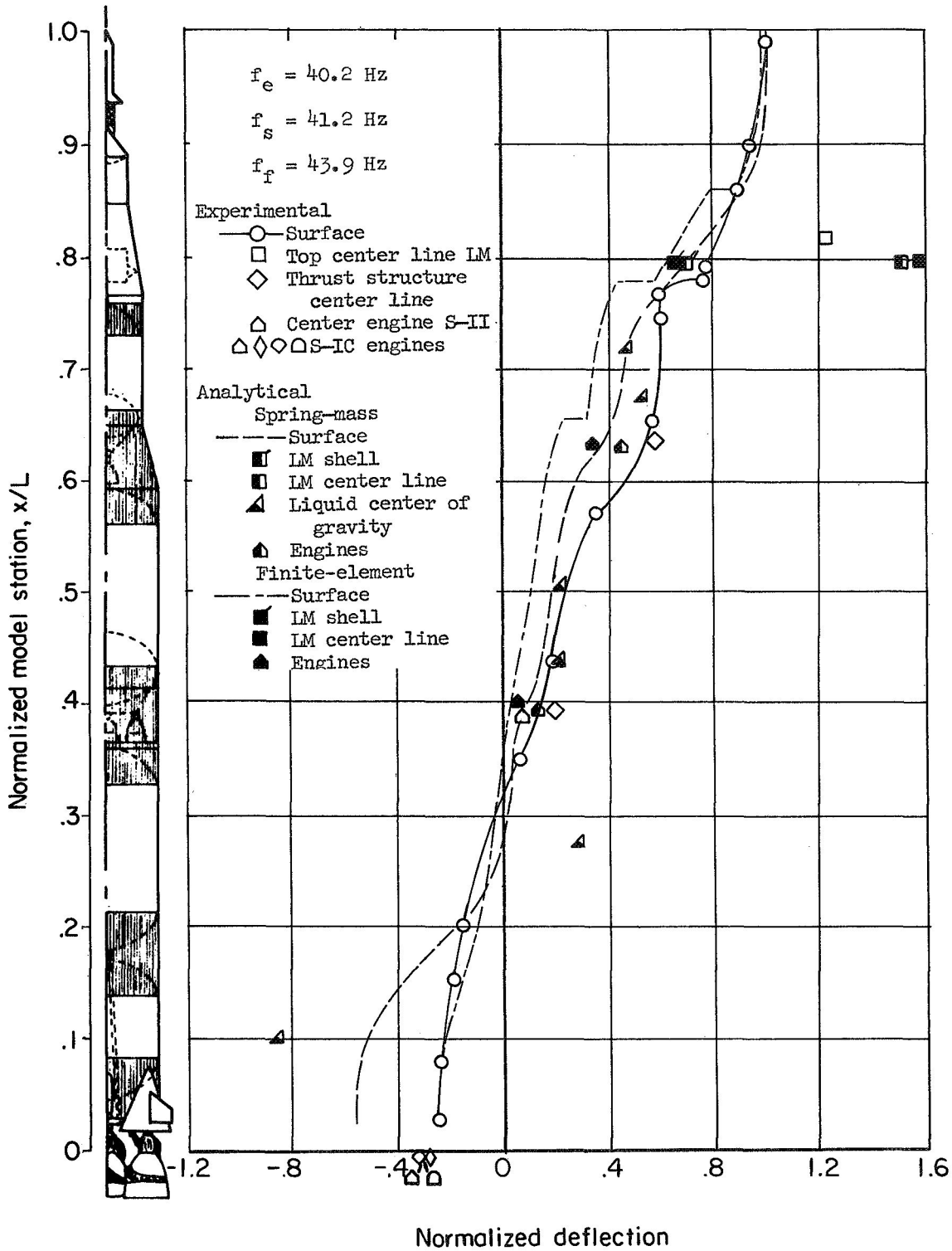

(a) 100-percent-weight condition.

Figure 15.- Experimental and analytical natural frequencies and mode shapes for first structural mode.

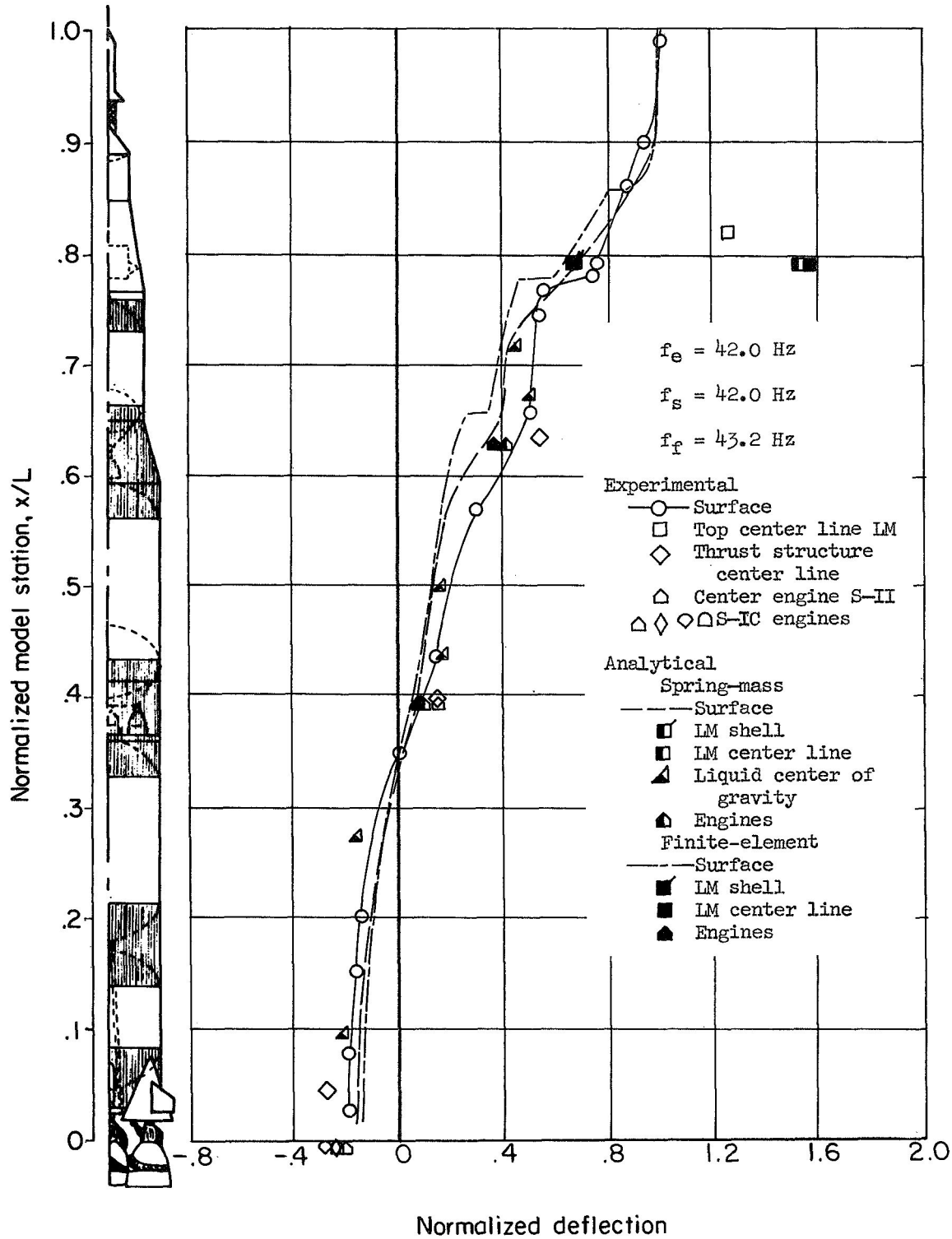

(b) 50-percent-weight condition.

Figure 15.- Continued.

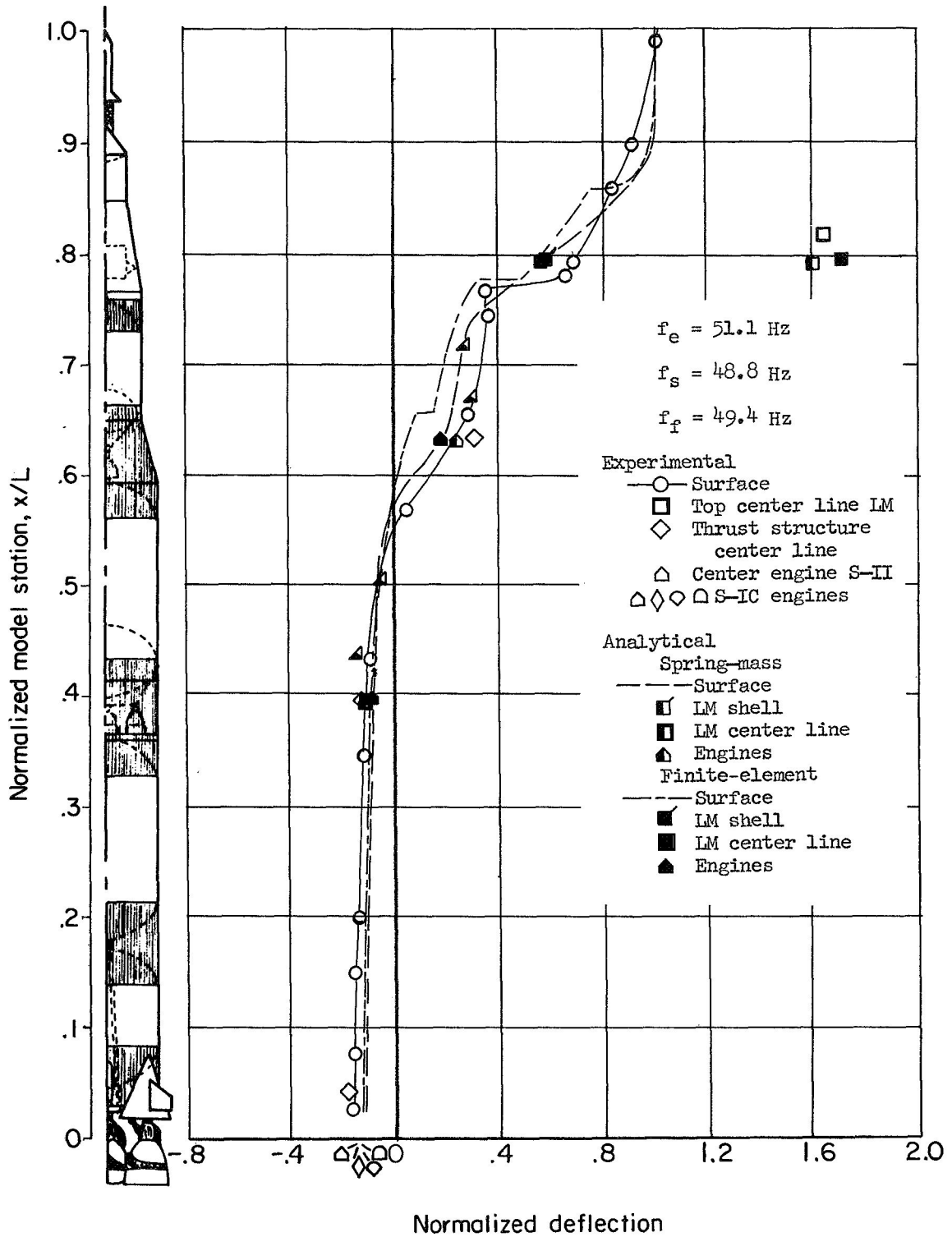

(c) Empty condition.

Figure 15.- Concluded.

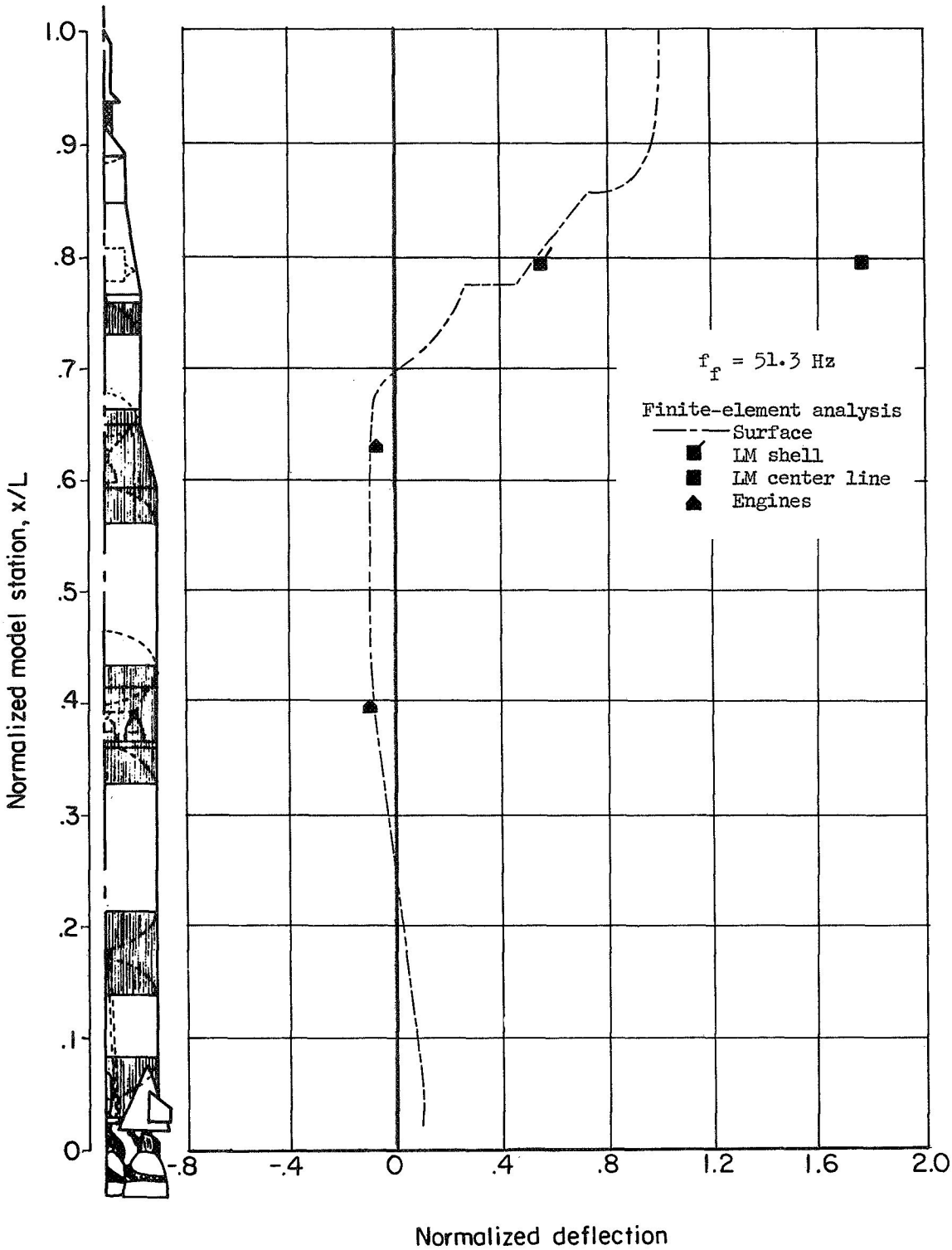

(a) 100-percent-weight condition.

Figure 16.- Natural frequencies and mode shapes for S-IVB fuel mode from finite-element analysis.

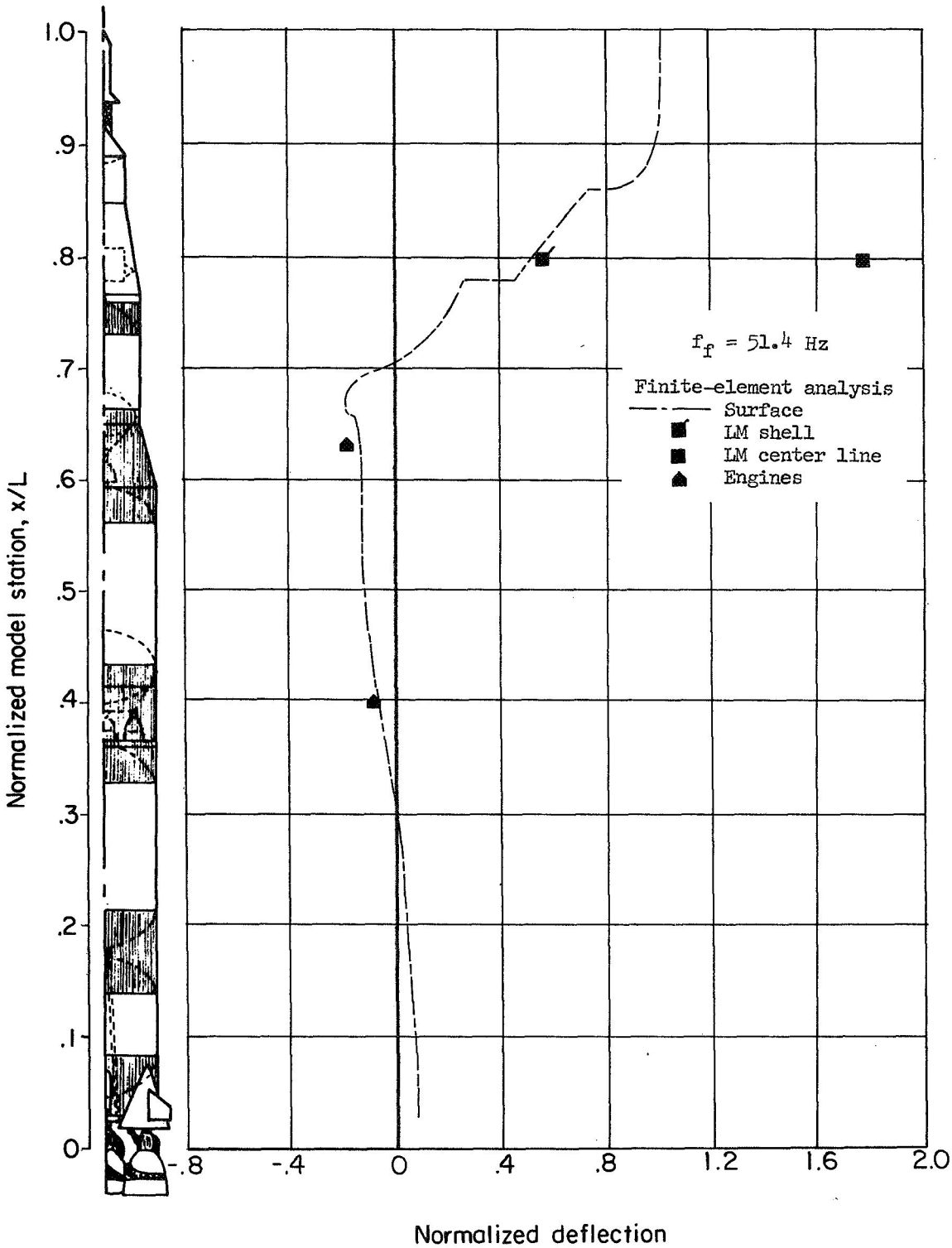

(b) 50-percent-weight condition.

Figure 16.- Continued.

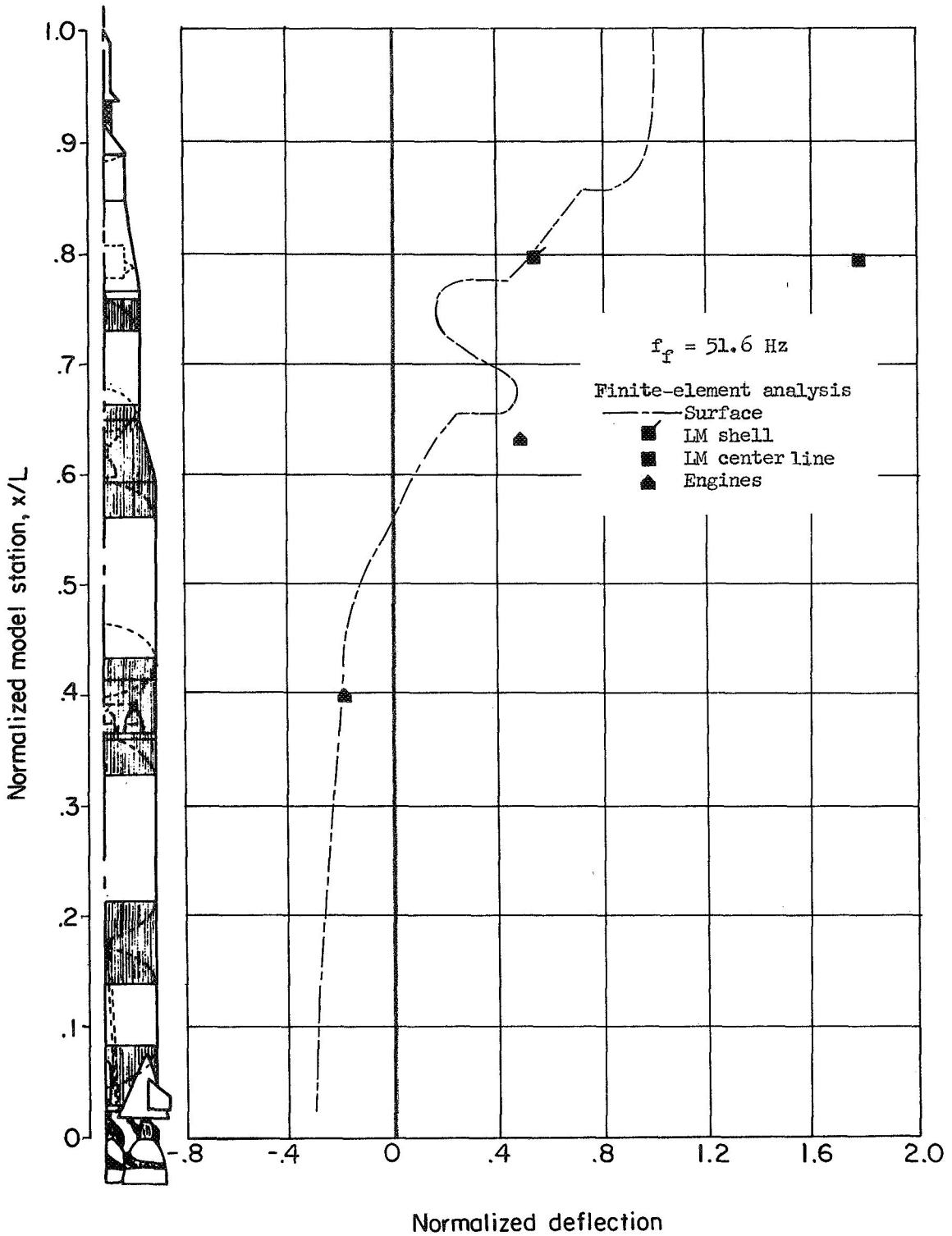

(c) Empty condition.

Figure 16.- Concluded.

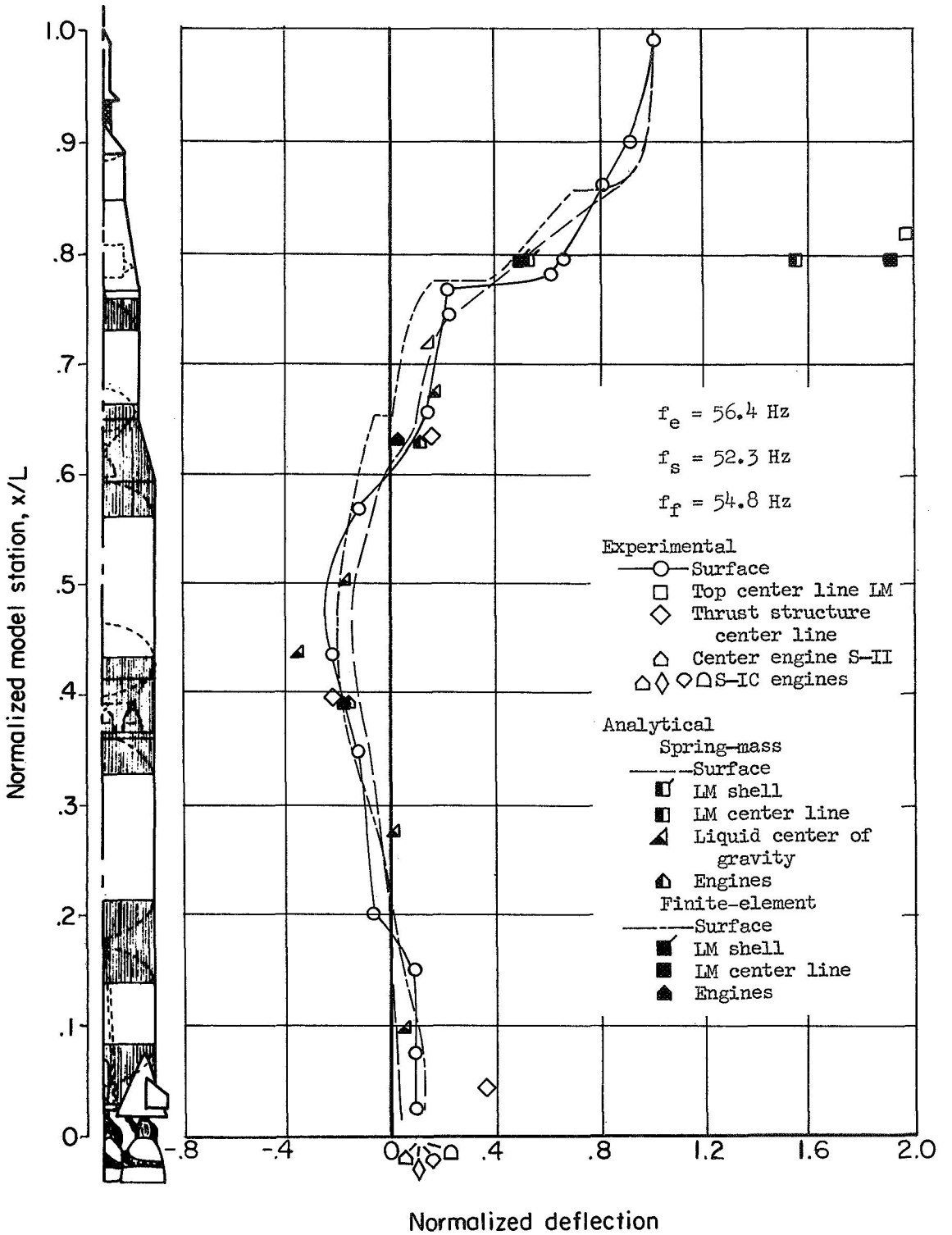

(a) 100-percent-weight condition.

Figure 17.- Experimental and analytical natural frequencies and mode shapes for second structural mode.

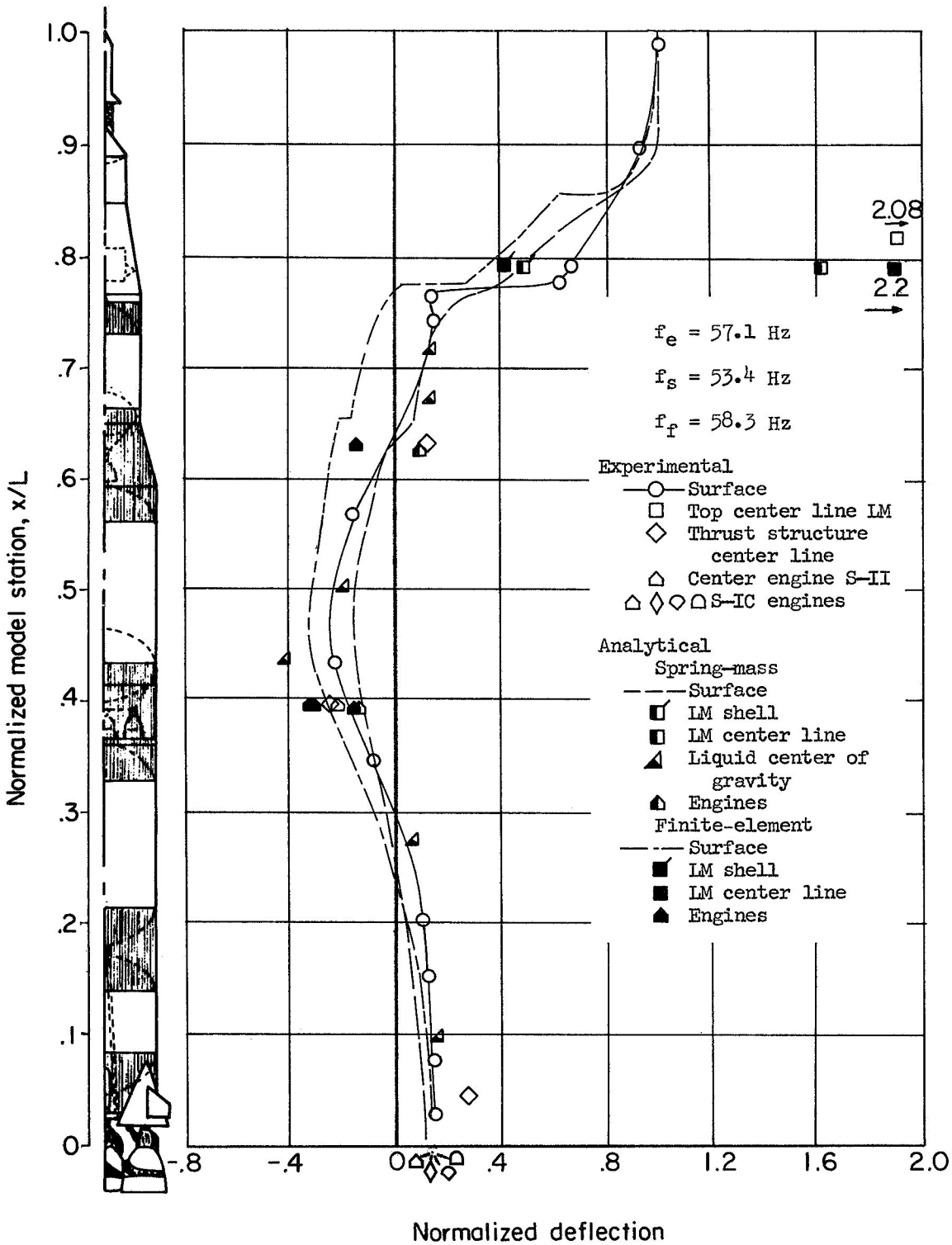

(b) 50-percent-weight condition.

Figure 17.- Continued.

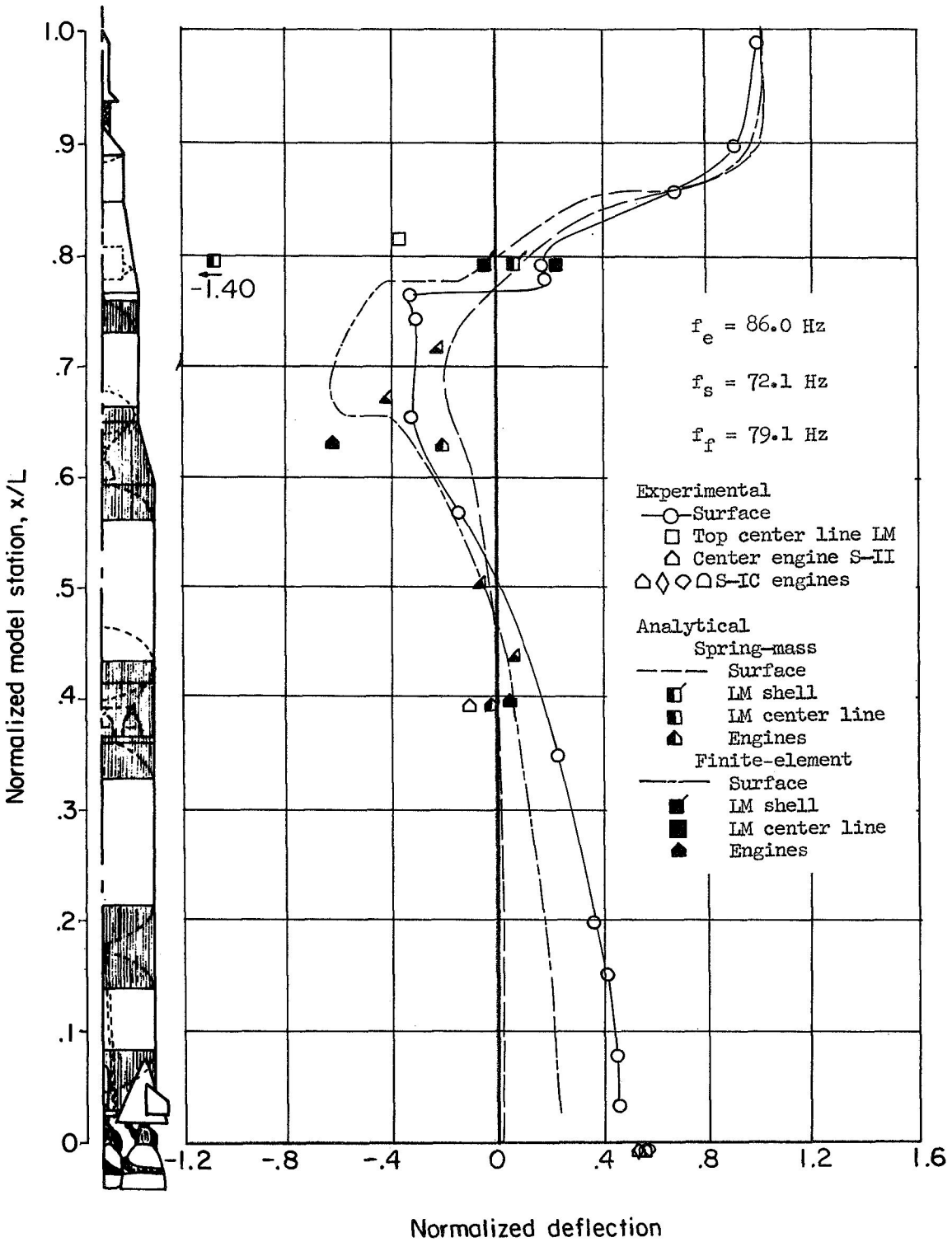

(c) Empty condition.

Figure 17.- Concluded.

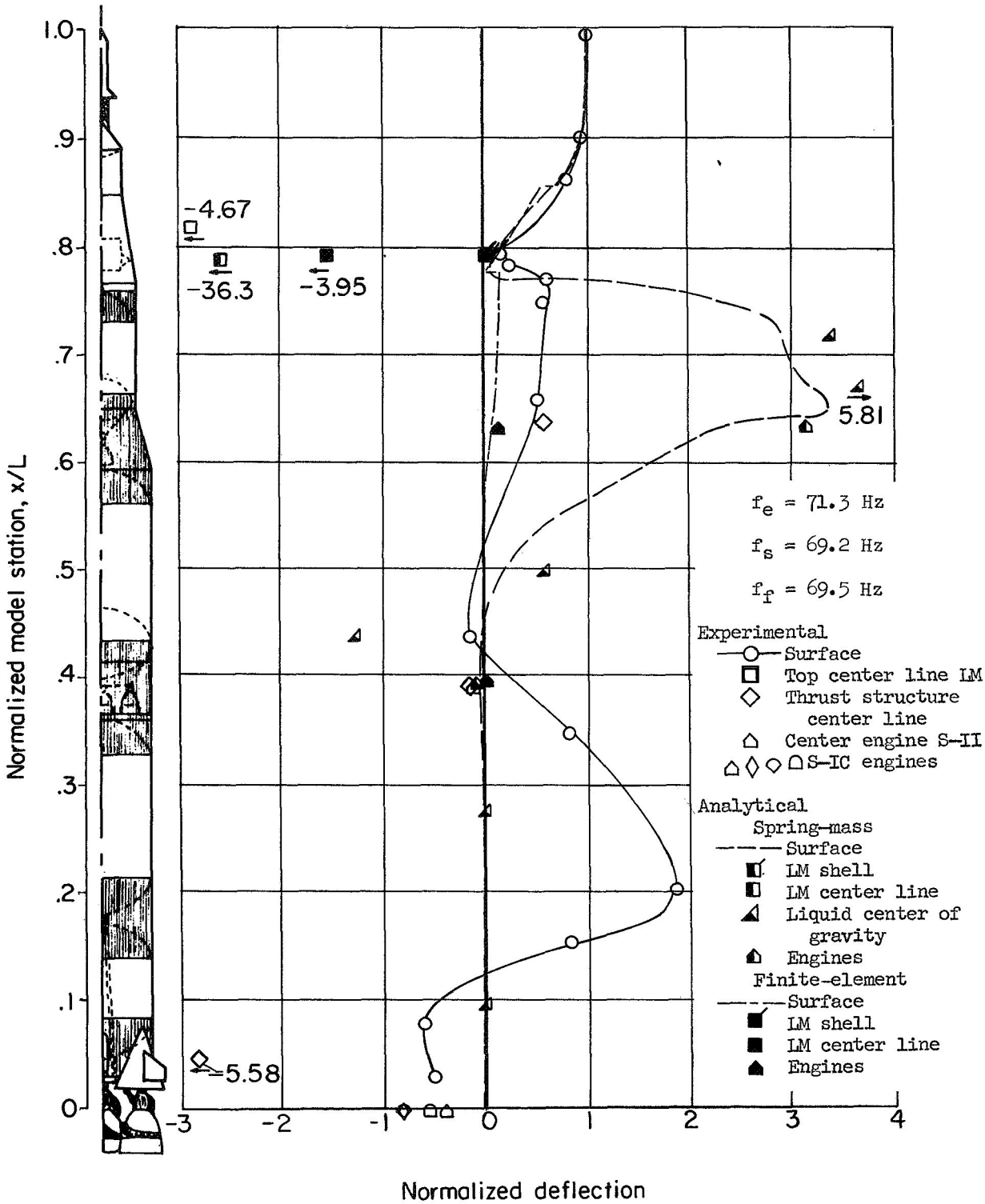

(a) 100-percent-weight condition.

Figure 18.- Experimental and analytical natural frequencies and mode shapes for LM mode.

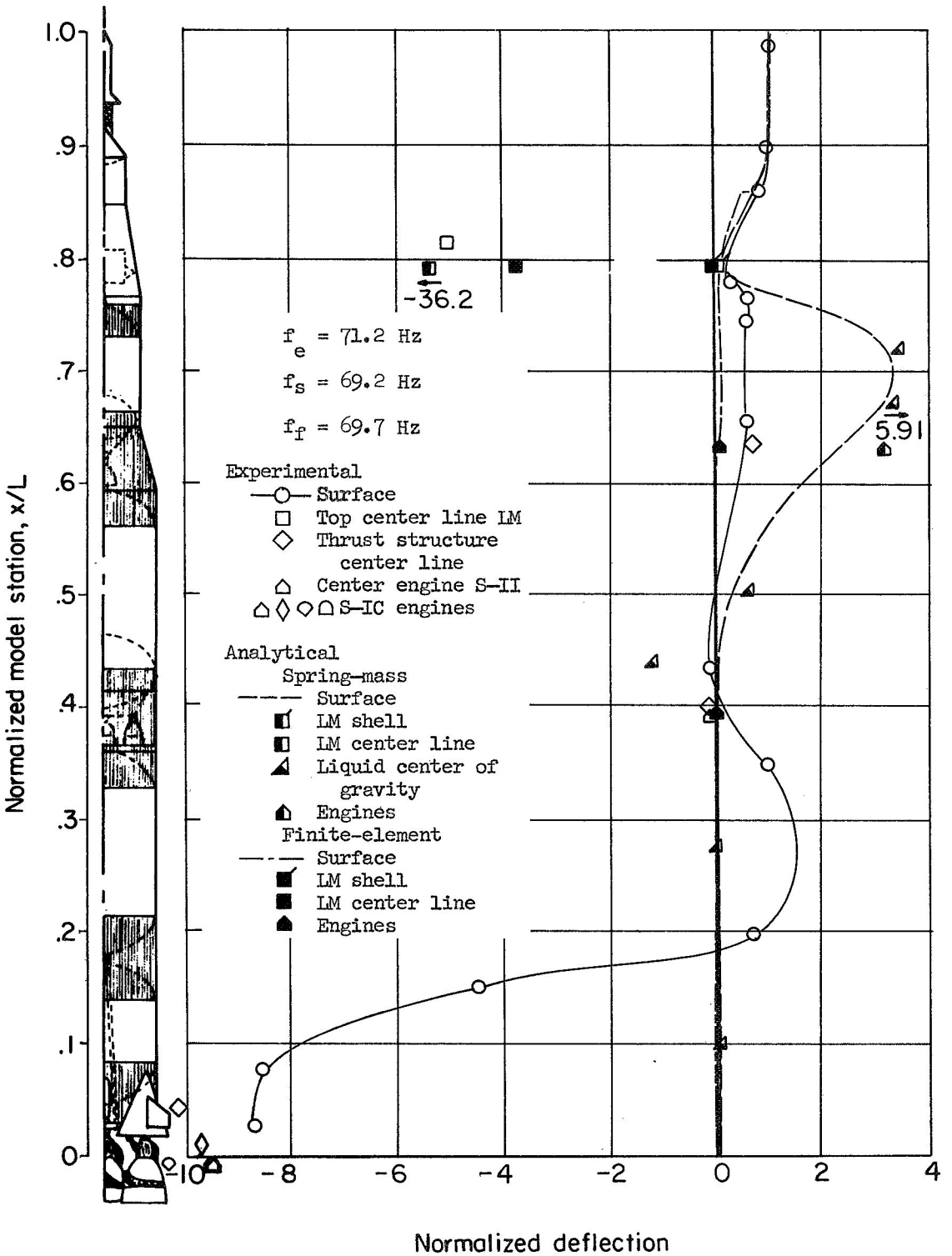

(b) 50-percent-weight condition.

Figure 18.- Continued.

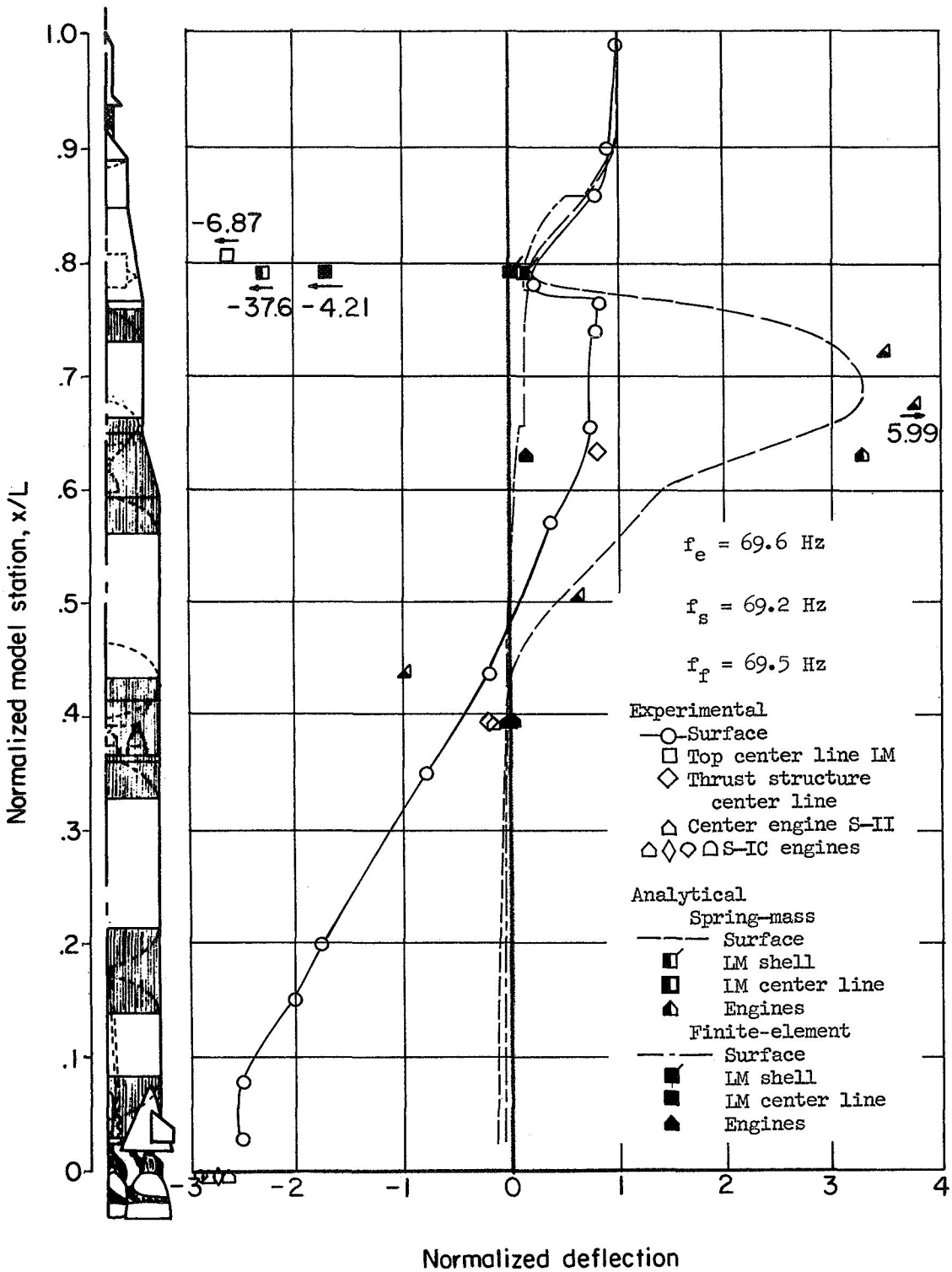

(c) Empty condition.

Figure 18.- Concluded.

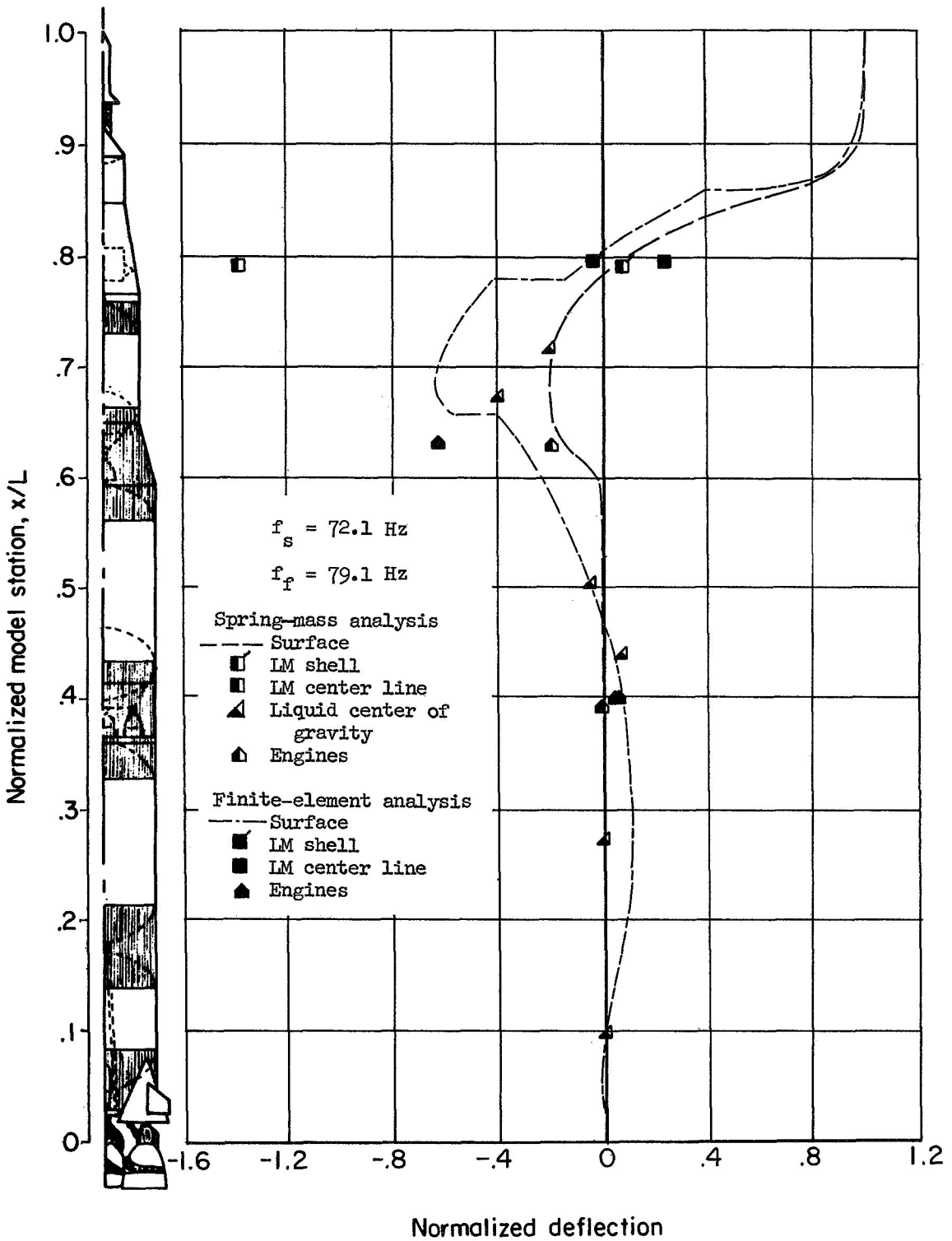

(a) 100-percent-weight condition.

Figure 19.- Analytical natural frequencies and mode shapes for third structural mode.

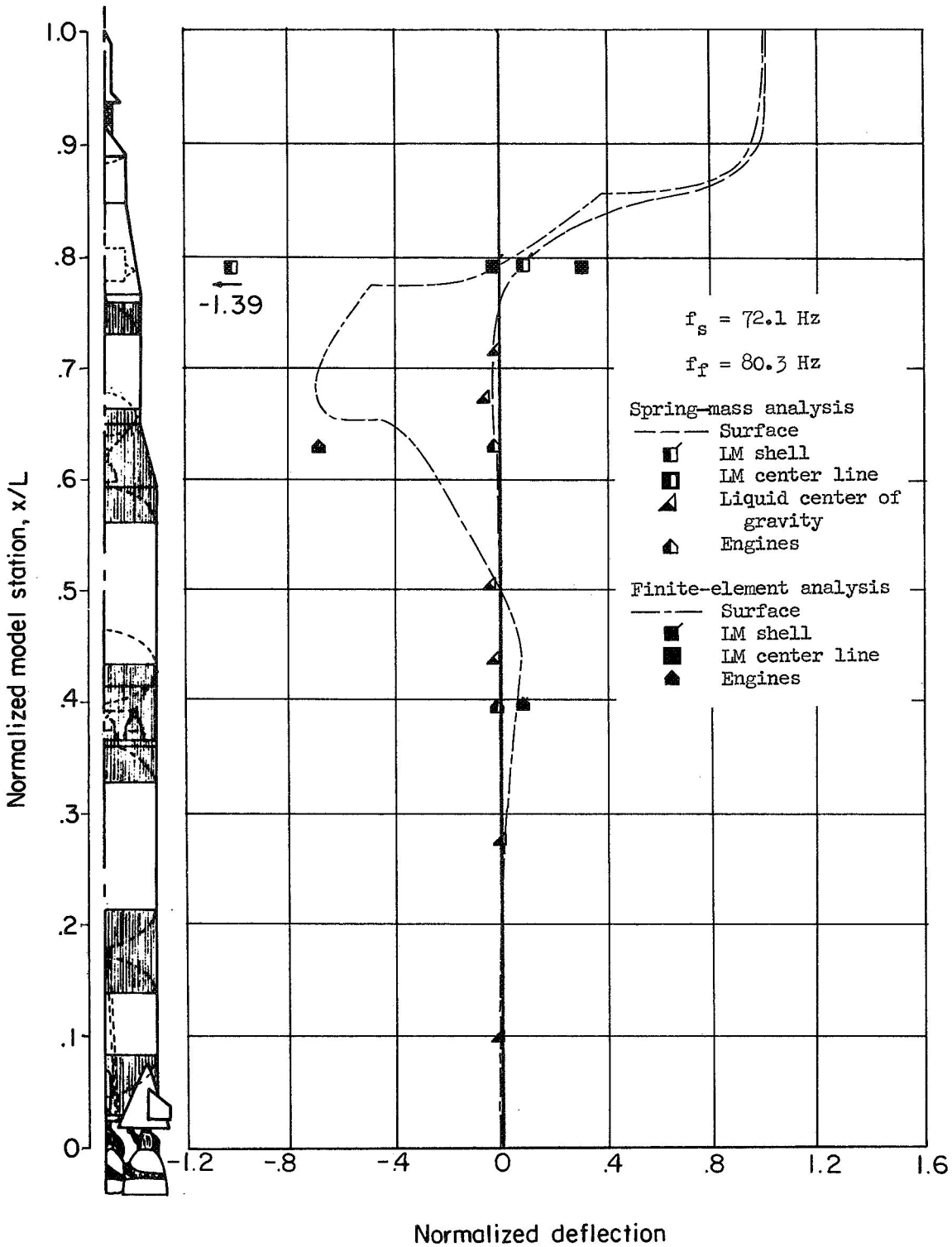

(b) 50-percent-weight condition.

Figure 19.- Continued.

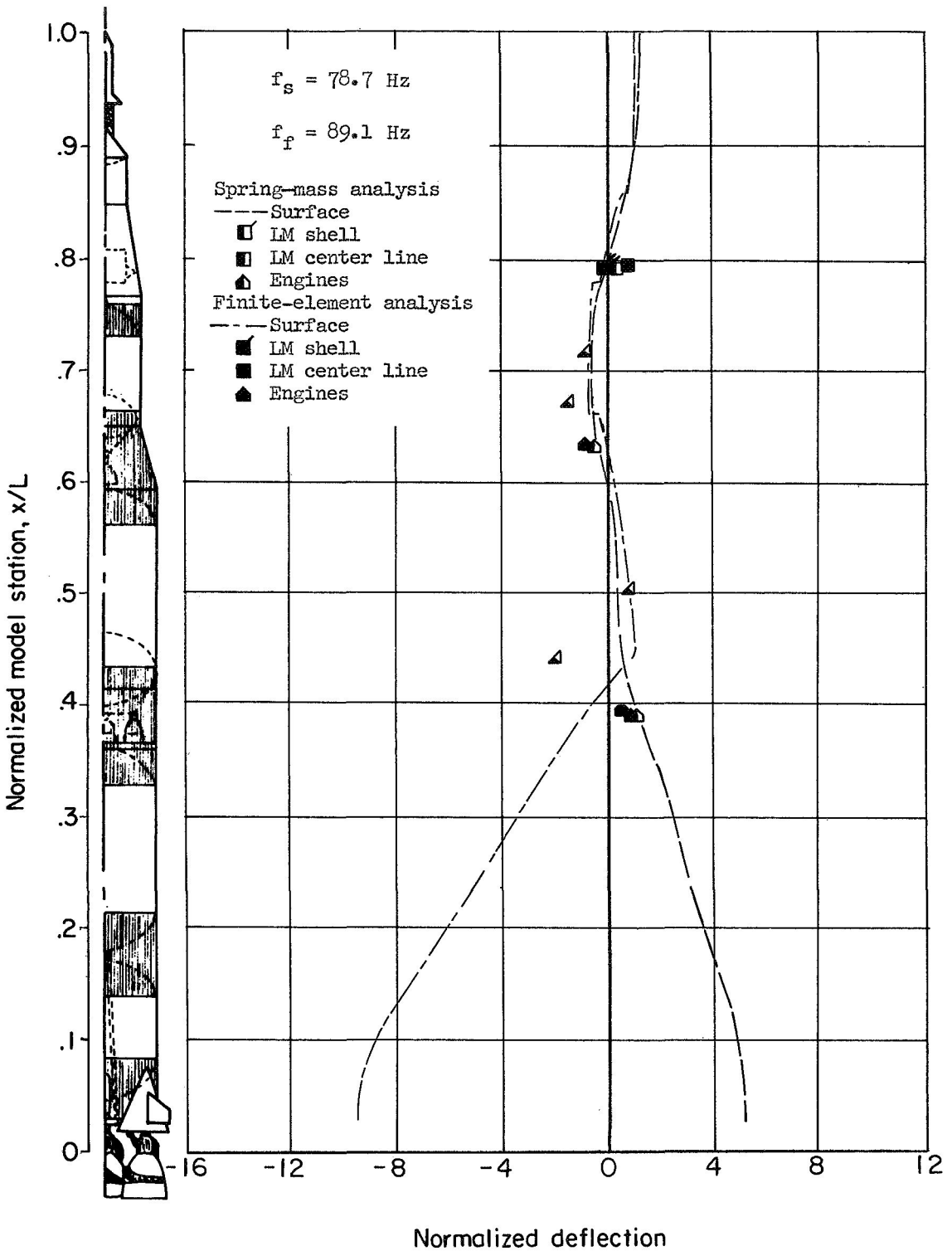

(c) Empty condition.

Figure 19.- Concluded.

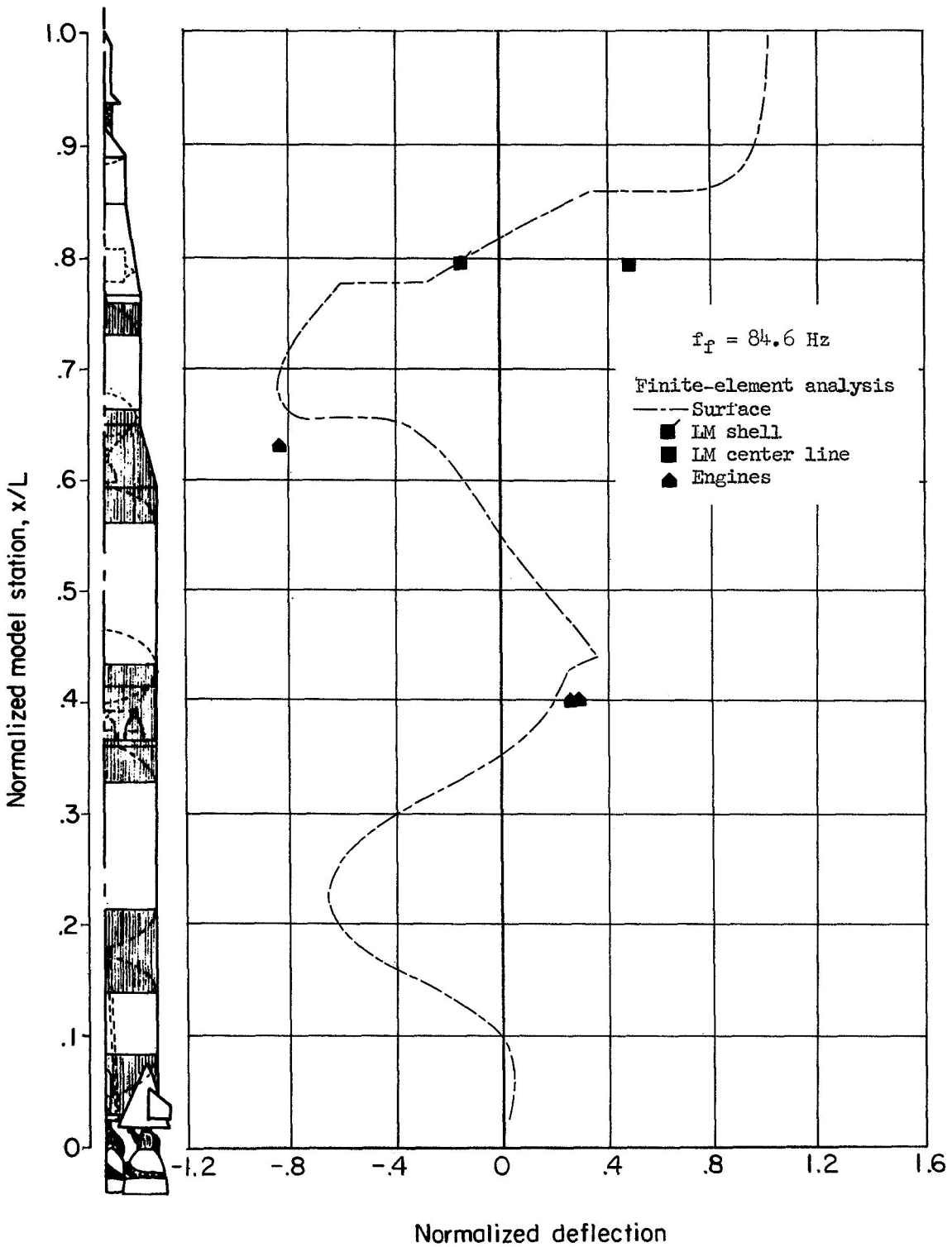

Figure 20.- Natural frequency and mode shape for second S-IC lox mode from the finite-element analysis for the 100-percent-weight condition.

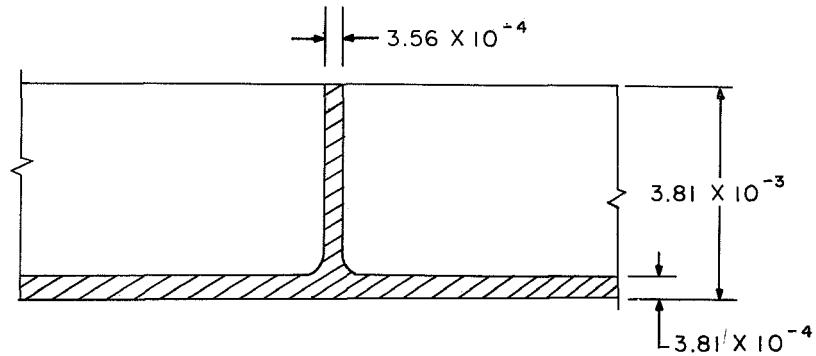

(a) Typical section along circumference.

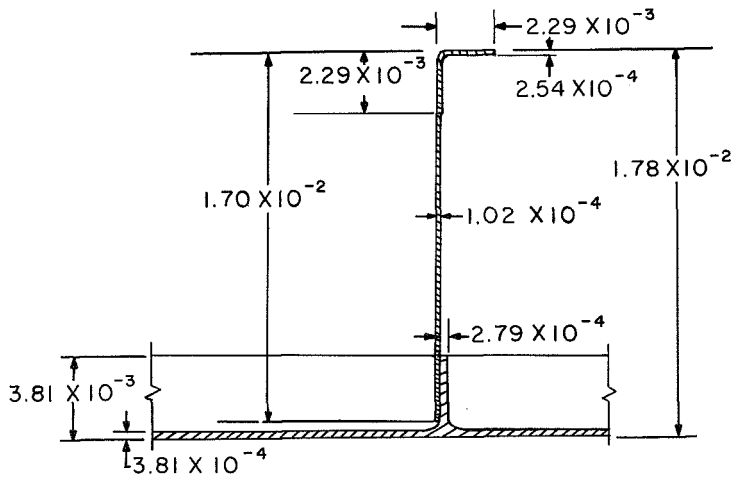

(b) Typical section along meridian.

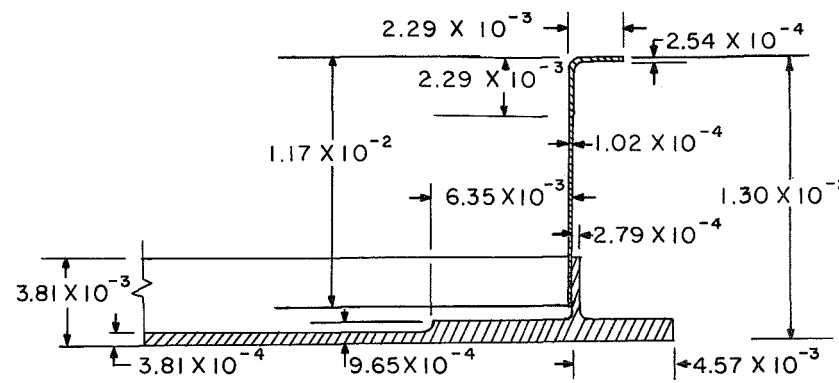

(c) Section along meridian showing aft end of cylinder.

Figure 21.- Details of S-II liquid hydrogen tank cylinder. (All dimensions are in meters.)

"The aeronautical and space activities of the United States shall be conducted so as to contribute . . . to the expansion of human knowledge of phenomena in the atmosphere and space. The Administration shall provide for the widest practicable and appropriate dissemination of information concerning its activities and the results thereof."

—NATIONAL AERONAUTICS AND SPACE ACT OF 1958

NASA SCIENTIFIC AND TECHNICAL PUBLICATIONS

TECHNICAL REPORTS: Scientific and technical information considered important, complete, and a lasting contribution to existing knowledge.

TECHNICAL NOTES: Information less broad in scope but nevertheless of importance as a contribution to existing knowledge.

TECHNICAL MEMORANDUMS: Information receiving limited distribution because of preliminary data, security classification, or other reasons.

CONTRACTOR REPORTS: Scientific and technical information generated under a NASA contract or grant and considered an important contribution to existing knowledge.

TECHNICAL TRANSLATIONS: Information published in a foreign language considered to merit NASA distribution in English.

SPECIAL PUBLICATIONS: Information derived from or of value to NASA activities. Publications include conference proceedings, monographs, data compilations, handbooks, sourcebooks, and special bibliographies.

TECHNOLOGY UTILIZATION PUBLICATIONS: Information on technology used by NASA that may be of particular interest in commercial and other non-aerospace applications. Publications include Tech Briefs, Technology Utilization Reports and Notes, and Technology Surveys.

Details on the availability of these publications may be obtained from:

SCIENTIFIC AND TECHNICAL INFORMATION DIVISION

NATIONAL AERONAUTICS AND SPACE ADMINISTRATION

Washington, D.C. 20546